SAND2018-9859R

A Laboratory Atom Interferometer Instrument

by

Rustin Nourshargh

A Mid-Course Assessment submitted to
the University of Birmingham

Ultracold Atoms Group
School of Physics and Astronomy
College of Engineering and Physical Sciences
the University of Birmingham

August 2018

Abstract

We have demonstrated a laboratory based, high bandwidth atom interferometer instrument and have performed an incipient gravity measurement with a fractional statistical uncertainty of $\sigma_g/g = 4.4 \times 10^{-6}$ where g is the acceleration due to gravity. We have designed, constructed, and optimised numerous laser systems for this purpose, most notably a powerful Raman laser (12 W at 780 nm) which will allow large momentum transfer and large detuning interferometry to be carried out at high bandwidth for the first time. This experiment is a general purpose test bed for exploring the fundamental limitations of atom interferometer techniques.

ACKNOWLEDGEMENTS

I'd like to thank my supervisor Grant Biedermann for both his expertises and generosity with his time, without which this project would not have succeeded as it did.

I am indebted to my colleague Adrian Orozco whose significant efforts before and during my placement were essential to the success of the project. I'm grateful for Jongmin Lee's expert supervision over many late nights which allowed me to meet the deadline. I'd like to thank Michael Martin for his insightful suggestions and willingness to discuss problems.

This work was carried out and Sandia National Laboratories and was funded in part by Sandia through the Laboratory Directed Research and Development program. This research exchange was enabled through a collaboration between University of Birmingham and Sandia National Laboratories[1].

[1]Sandia National Laboratories is a multimission laboratory managed and operated by National Technology & Engineering Solutions of Sandia, LLC, a wholly owned subsidiary of Honeywell International Inc., for the U.S. Department of Energys National Nuclear Security Administration under contract DE-NA0003525.

CONTENTS

CHAPTER 1

INTRODUCTION

1.1 Light Pulse Atom Interferometry

Light pulse atom interferometry is a technique exploiting the fundamentally quantum nature of atoms to make extremely sensitive measurements. In 1924 Louis de Broglie postulated that all matter has both particle and wave properties.[1] We are able to use matter waves of cold atoms to generate an interference pattern in a device called an atom interferometer. This interference is equivalent to the optical fringe pattern observed in Michaelson interferometer. Whilst a traditional interferometer uses physical mirrors and beam splitters, for an atom interferometer we use laser pulses to split and recombine atomic waves. The first laser pulse divides the atom wave into two interferometer paths which are spatially separated. Further laser pulses reflect and then recombine the two paths. After recombination the atoms are measured. Each atom has a probability of being measured in one of two states (electronic energy levels). This probability depends on a quantity called phase which is accumulated between the arms of the interferometer. This phase difference depends on the potential the atoms move through. Gravitational and electromagnetic fields both produce such potentials, and the laws of relativity tell us that accelerations and rotations can also me measured. Modern laser systems allow exquisite control of atomic states, and we can measure these quantities with beyond state of the art sensitivities.

The high sensitivities achieved by atom interferometers are pushing the boundaries of fundamental physics. Current experiments being pursued include measurement of the fine structure constant, probes of QED, redefining the mass standard, limit deviations from standard Model, beyond general relativity 5th force measurement, gravitational Aharonov Bohm effect, and the weak equivalence principle. Some of these experiments are at the current state of the art and will surpass it in the near future.[2][3][4][5][6]

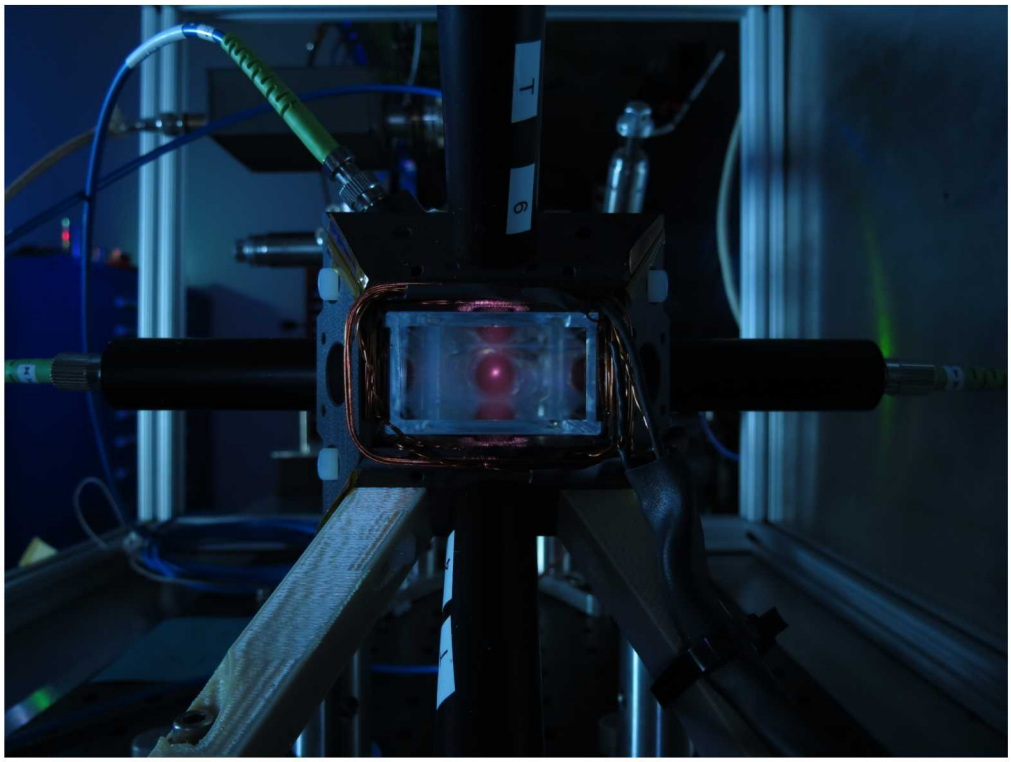

Figure 1.1: A magneto-optical trap (see red dot) in the centre of the completed atom interferometer.

1.2 Accelerometers and Gravimeters

The equivalence principle tells us that acceleration and the force due to gravity are indistinguishable with local experiments, and as such their their measurements are equivalent.[7] Practical devices differ radically in dynamic range and sampling rate, and as a result sensitivity.

1.2.1 Accelerometers

Accelerometers have a wide range of applications including inertial navigation, image stabilisation, structural monitoring, healthcare, gaming, and many more. Ease of manufacture and reduced costs have allowed MEMS (Micro Electro Mechanical System) based devices to pervade the consumer electronics industry, and rapid enhancements are expanding the range of applications.[8] Some of the most demanding requirements are found in inertial navigation systems (INS), which are receiving renewed interest with the development of autonomous vehicles. INS are typically deployed in dynamically varying environments, and can be subject to shock, vibrations, rotations, and accelerations in any direction. They are commonly required to measure both positive and negative accelerations, with some specialist applications requiring high sensitivity across

ranges as large as $\pm 1000g$. Whilst MEMS sensors are versatile they do have limitations, most notably in their bias stability. For a MEMS sensor this is limited by the mechanical stability of the test object, typically a cantilever, making some level of drift inevitable. INS applications are critically dependant on temporal resolution and bias stability. Small bias drifts lead to errors which grow quadratically in time and provide a fundamental limit on the accuracy that an open loop INS can achieve.[9] Atom interferometers could increase the performance of such systems and accelerometers have been demonstrated that can operate at the $\mu g/\sqrt{\text{Hz}}$ and 100Hz.[10][11][12] Despite this success there are many technical challenges to be solved before an AI based accelerometer can beat the state of the art. Atom interferometers will need to meet stringent size, weight, and power requirements in challenging environments before they can be integrated into most INS applications. These challenges are beyond the scope of this laboratory based project, and as such we will not discuss accelerometers any further.

1.2.2 Gravimeters

Gravimeters are typically employed in static environments, where some degree of vibration isolation is possible, and they are only required to measure in a single direction; down. They do not need to tolerate, or measure, accelerations orthogonal to the measurement direction. Across the entire earth's surface the acceleration due to gravity varies by less than 1%, and gravimeters can be optimised for high sensitivity in this very narrow range. A much lower measurement bandwidth is often acceptable.

Gravimeters have numerous applications including mineral exploration and extraction, sinkhole detection, location and assessment of infrastructure (pipes, water), subsidence prevention (detecting cavities), surveying disused mineshafts, water resource management, navigation, archaeology, border control, and security.[13] As a sensing technique gravimetery is unique; gravity cannot be shielded and has infinite range. Some tasks can be achieved with ground penetrating radar (GPR) but it has it's limitations. Water in the medium can lead to difficulty in interpreting results and GPR is unable to detect anything through high conductivity media such as reinforced concrete, metallic structures or clay soils.[14] By contrast gravimeters measure the density profile of the subsurface, regardless of medium.

Conventional gravimeters are typically divided into two types, relative and absolute gravimeters. Relative gravimeters are able to measure fractional changes in g with high precision, but are not able to provide absolute values with any useful accuracy. The most common systems measure the extension of a mass on a spring; with a known spring constant g can be calculated. The temperature of the spring and the influence of external vibrations must all be precisely controlled to maintain consistent performance. The difficulty in

measuring the spring constant with sufficient accuracy restricts these devices to relative measurements; i.e. observing small fractional changes from a reference point. For many applications a relative measurement is sufficient, including most surveys where the data is taken over a short time period (days or weeks) in a limited geographic location. An existing commercial relative gravimeter is the CG-6 from Micro-g LaCoste, demonstrating repeatability 5μGal; uncorrected drift $< 200\mu$Gal/day.

Some applications require absolute measurements. Gravity maps for inertial navigation, and surveys requiring stability over long time periods (hydrocarbon monitoring) are important examples of this. Conventional absolute gravimeters typically measure the trajectory of a test mass in free-fall. One such device, the Scintrex FG5-X, uses a reflector under free-fall in a vacuum as one arm of a Michelson interferometer. The time evolution of the interferometer fringe pattern is a sensitive probe of g. The FG5-X achieves $15\mu\text{Gal}/\sqrt{\text{Hz}}$ in a controlled laboratory setting (2μGal accuracy). In real surveys, micro-seismic noise requires averaging for several minutes before μGal sensitivities can be achieved. Repeated dropping of the test mass results in mechanical wear on the system, with maintenance required after as little as 100 hours of operation. Challenging environments limit this lifetime further. To prolong instrument life it is commonly used at much lower measurement rates of 1/15 Hz or less and the achieved sensitivity falls to $100\mu\text{Gal}/\sqrt{\text{Hz}}$.[15] A portable version of the FG5, can reach a precision of 10μGal in 10 minutes at a 'quiet site' but will require significantly longer to reach this precision in many real surveys. This long averaging time has limited their widespread use. Atom interferometers can employ several techniques to effectively remove the need for this averaging time. Laboratory interferometers have already surpassed conventional sensors in sensitivity and bias stability.[16] Portable sensors are being developed and will surpass conventional sensors in both reliability and measurement rate. These enhancements will allow gravimeters to be routinely employed in a much wider range of applications.

In this report we discuss the development of a laboratory based, high bandwidth, atom interferometer for gravimeter. This instrument includes the unique combination of powerful laser systems and high bandwidth optimisations which will allow new operating regimes to be explored.

CHAPTER 2

INTERFEROMETRY THEORY

This chapter is a very brief summary of the theory underpinning an atom interferometer and stimulated Raman transitions. In areas where this experiment differs from the norm, additional explanations are included. Detailed explanation can be found in the following references.[17][15][18]

2.1 Raman Transitions

Stimulated Raman transitions are coherent two-photon processes that allow long lived ground states to be coupled through the use of an intermediate state. With appropriate choice of intermediate state this can be accomplished with near perfect fidelity and the resulting system behaves like an ideal two level system. By controlling the duration, power and detuning of these photons coherent superposition of the two states can be generated. The other important fact is that if the two photons are initially counter propagating, then this two-photon process imparts a momentum of $2\hbar k$ to one of the two atomic states. The uses of this will be discussed in section 2.2.

The following equations underpin the key properties of Raman transition and inform our laser system requirements. In the following discussion I will refer extensively to the Rabi frequency, this is the radian frequency at which the atom oscillates between two states under in influence of a given light field. A π-pulse is a laser pulse of the exact duration required to drive half of a Rabi oscillation, or to completely transfer population from one state to the other. Equation 2.1 relates the effective Rabi frequency for a Raman transition (Ω_{eff}) to the Rabi frequencies for each of the two resonant optical transitions and the single-photon detuning (Δ). These Rabi frequencies are a property of both the atomic transition and the applied light field. The most important feature of this equation is that the Rabi frequency is inversely proportional to the single-photon detuning Δ; large detunings result in low Rabi frequencies and correspondingly long

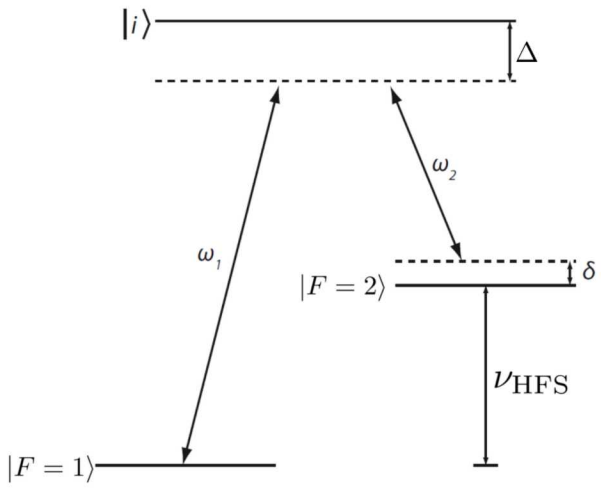

Figure 2.1: Stimulated Raman transitions coherently couple the two ground state levels through the use of an intermediate excited state. The atomic energy levels of Rb^{87} are shown with solid lines. The intermediate state is shown as a dashed line, detuned from $|i\rangle$ by the single-photon detuning Δ. The two-photon detuning is labelled δ. Adapted from Schmidt.[15]

π-pulses.

$$\Omega_{\mathrm{eff}} = \frac{\Omega_1 \Omega_2}{2\Delta} \tag{2.1}$$

Equation 2.2 states that the effective Rabi frequency is proportional to the root of the intensity in each of the two Raman beams. This means that for a fixed optical power, the highest Rabi frequency is achieved when the intensities of two beams are equal. It also tells us that in this equal power mode, Ω_{eff} is proportional to total laser power. Powerful laser systems are therefore needed to realise large Rabi frequencies and short π-pulses.

$$\Omega_{\mathrm{eff}} \propto \sqrt{I_1 I_2} \tag{2.2}$$

Equation 2.3 relates the probability of spontaneous emission from the excited state $\mathcal{R}_S$ to the single-photon detuning Δ. Such emission causes an atom to be lost for our interferometer and results in lower pulse efficiencies. For a standard 3-pulse interferometry sequence this is not usually a limitation as even 60% pulse efficiency still allows 36% of atoms to complete an interferometer. This can be achieved with modest detunings $\sim$GHz. As this loss scales arithmetically with the number of laser pulses, large momentum transfer interferometers utilising many pulses require much higher efficiencies; they operate at large detunings.

$$\mathcal{R}_S \propto \frac{1}{\Delta^2} \tag{2.3}$$

The final equation relates the effective Rabi frequency to the temperature range of atoms that can be addressed by a π-pulse at that frequency. The linewidth of these two-photon transitions is very narrow, and as such the frequency width of the pulse is limited by the pulse duration through a Fourier transform. At high Rabi frequencies, the π-pulses are short and as such address a relatively broad frequency and therefore temperature class of atoms. All experiments are fundamentally limited by the atom shot noise limit so increasing the atom number will increase sensitivity.

$$T_{\text{Doppler}} \propto {\Omega_{\text{eff}}}^2 \tag{2.4}$$

2.2 Mach-Zehnder Interferometry

In light pulse atom interferometer, the beam splitters and mirrors are generated by controlled pulses of light. Whilst numerous geometries and approaches have been demonstrated we will focus on the Mach-Zehnder interferometer with Doppler sensitive Raman transitions. The pulse scheme is shown in figure 2.2.

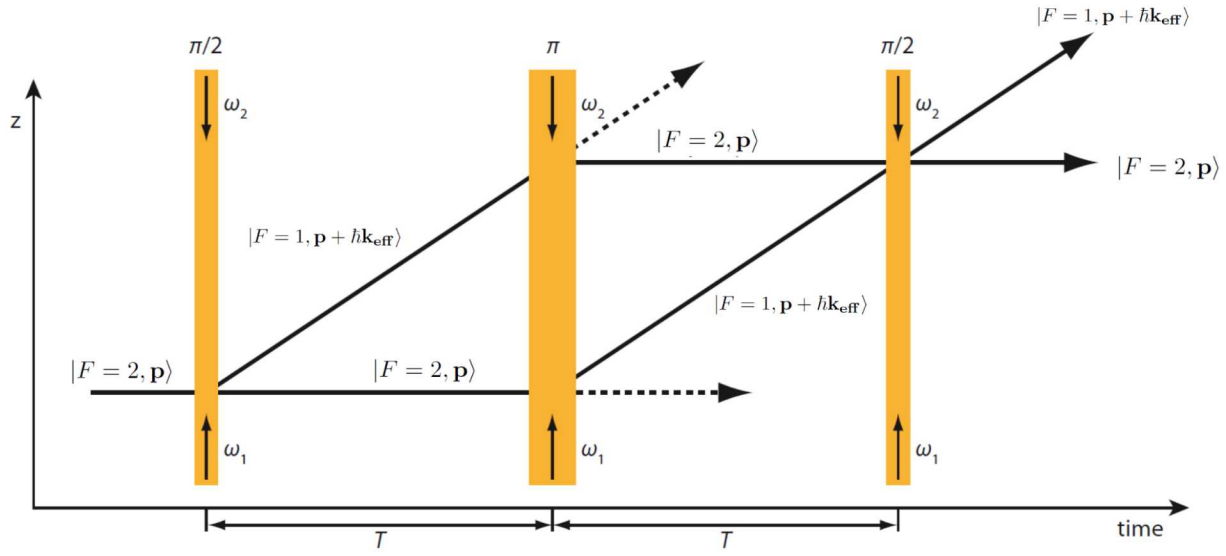

Figure 2.2: This diagram illustrates the atomic and momentum states for the two paths through the interferometer. Laser pulses are shown in orange. Adapted from Schmidt.[15]

The first pulse acts as a beam splitter ($\pi/2$-pulse) creating a superposition between the two atomic states

and transferring $\hbar k_{\text{eff}}$ of momentum to the F=1 superposition. After the interrogation time T has elapsed a mirror pulse (π-pulse) transfers the atoms into the opposite superposition. $\hbar k_{\text{eff}}$ of momentum is imparted to F=2 and the $\hbar k_{\text{eff}}$ originally transferred to F=1 is imparted back into the light field. The final beam splitting pulse ($\pi/2$-pulse) closes the interferometer. The state of the atoms is measured typically with fluorescence, and the fraction of atoms in each of the two states is found. This ratio is found to depend on the phase difference between the interferometer paths. This phase is itself a very sensitive probe of the environment the atoms travel through. In the case of accelerations or gravity the relevant contribution varies with equation 2.5. Where T is the interrogation time, t_π is the duration of a π-pulse, k_{eff} is the effective wavevector of the Raman transition ($4\pi/\lambda$ for a simple Raman beam splitter) and g is the acceleration due to gravity.

$$\Delta\phi = -\mathbf{k_{eff}} \cdot \mathbf{g} \left[T^2 + t_\pi \left(1 + \frac{2}{\pi} T \right) \right] \tag{2.5}$$

The quadratic term quickly dominates the phase. This quadratic dependence in T would suggest longer interferometers being more sensitive. Everything else being equal resolution would increase with $T^{3/2}$. In a fixed observation period (τ) one can take N measurements of duration T, giving a resolution of $R \propto \sqrt{N} T^2$ (averaging of uncorrelated measurements increases resolution with $\sqrt{N}$). $N \propto \tau/T$ (at constant duty cycle) so the resolution scales with $R \propto \sqrt{\tau T^3}$, which for a fixed measurement window gives $R \propto T^{3/2}$. Whilst the most sensitive instruments do exploit T times in excess of a second, this requires metres of freefall, highly optimised cooling, and generally results in small numbers of atoms.

The other way to increase sensitivity is by increasing k_{eff}. This can be achieved by combining multiple groups of Raman pulses requiring higher pulse fidelities to maintain contrast. Other approaches including Bloch oscillations and Bragg diffraction have shown enhanced sensitivities in systems operating at long T times. Both approaches require higher laser powers and typically require lower atom temperatures than a standard Raman interferometer. The instrument constructed in this report will be able to investigate whether these techniques can be applied at high-bandwidth; this is beyond the scope of this document.

2.3 High Bandwidth Interferometry

The instrument constructed in this work operates at high bandwidth $>$ 40Hz and this is interesting for a number of reasons. At short T times the atoms cannot travel a large spatial distance; this allows efficient recapture and a large reduction in down time between measurements. The instrument can also be very physically compact with a 10ms freefall only travelling 0.5mm compared with the 1.25m required for a 0.5s

drop. The short T time also relaxes the constraints on atomic cloud temperature. A cloud of a higher temperature will remain within the Raman beams during the interferometry sequence simply because they have insufficient time to leave. This reduces the requirements on laser cooling, and allows us to address a much broader velocity class of atoms. Atom interferometers typically have to employ velocity selection and blow-away pulses to retain contrast during interferometry. Our short T time removes the need for these and with sufficiently powerful Raman beams, a significant fraction of the atoms within the MOT are able to participate. All interferometers are fundamentally limited by atom shot noise, and if the technical challenges can be met to allow the instrument to operate at that level, then these large increases in atom number will allow high bandwidth systems to achieve very high sensitivities. Large atom numbers, short dead times, and compact instrument sizes all make high bandwidth interferometry a very promising technique for future sensors.

2.4 Raman Beams generated by Modulation

We generate the frequencies for our Raman beams with an EOM (electro-optic modulator) operating at 1560nm, the output of which is amplified and then frequency doubled. Using an EOM to generate our Raman frequencies has advantages. The EOM adds frequency sidebands to a carrier. The relative spacings and amplitudes of these sidebands are controlled by the frequency and amplitude of an RF input. It is possible to control these RF signals to <1Hz in GHz signals with COTS (commercial off-the-shelf) components, meeting the system requirements without any custom RF circuit design.

In our system we drive the EOM at the atomic Hyperfine splitting (after compensating for AC-stark shifts) and adjust the RF power to make the carrier and 1st sideband powers equal in amplitude as measured at 780nm. Second harmonic generation (frequency doubling) doubles the modulation depth but leaves the sideband spacings unchanged; the RF used to drive the EOM allows for this. We have now generated three laser lines of equal power, separated by the hyperfine splitting ν_{HFS}; this is sufficient to drive Doppler-free Raman transitions from a single interferometry beam (see section 7.2).

We deliver all three of these frequencies to the atoms through both fibres (section 4.3). For a Doppler sensitive (gravity sensing) interferometer at high bandwidth this creates a problem. We cannot use the Doppler effect to break symmetry between the Raman beams propagating in opposite directions. For the interferometer to function successfully it is vital that each atom takes the same photon from each beam. For example, if we wish our first pulse so cause the atom to recoil upwards, it must absorb an upward going photon and emit a downward going photon. Without breaking this symmetry we will scatter photons in both

directions, and from a single beam, resulting in at least two simultaneous Doppler sensitive and two Doppler insensitive interferometers. After three interferometry pulses the number of possible outputs will make any results near impossible to interpret, and very much less sensitive than the simple 2 beam case.

For our Doppler sensitive (gravity measuring) interferometer we break this symmetry by increasing the splitting between the sidebands by 74MHz and then passing one of the two Raman beams through an AOM also operating at 74MHz. This guarantees that only interferometers scattering in one direction meet the frequency condition, (the 150MHz frequency offset in the opposite direction make this transition probability negligible).

Even with the AOM, the presence of three frequencies in each beam results in two pairs of beams able to drive an interferometer in the desired direction (differing in Δ by the modulation frequency $\nu_{\mathrm{HFS}} + 74\mathrm{MHz}$). Fortunately this is not a problem, both pairs of beams drive coherent transitions and we can simply sum the Rabi frequencies of each beam pair to find the total Rabi frequency. In practice for small detuninings $6.8\mathrm{GHz} \gg \Delta$ the pair with the smaller detuning will dominate, where as for large detunings $6.8\mathrm{GHz} \ll \Delta$ the contributions become almost equal. Raman transitions will be driven with intermediate states detuned from all available levels. Generally the one with the strongest coupling strength or largest detuning will dominate, but again all contributions must be summed for a precise calculation of the Rabi frequency. In practice the Rabi frequencies are not normally calculated theoretically, and instead we measure it experimentally and use the scaling rules described in the equations in section 2.1 to predict the effect of changes in experimental parameters.

CHAPTER 3

SYSTEM DESIGN

The following section outlines sensor head design with particular focus on features that enable high bandwidth operation.

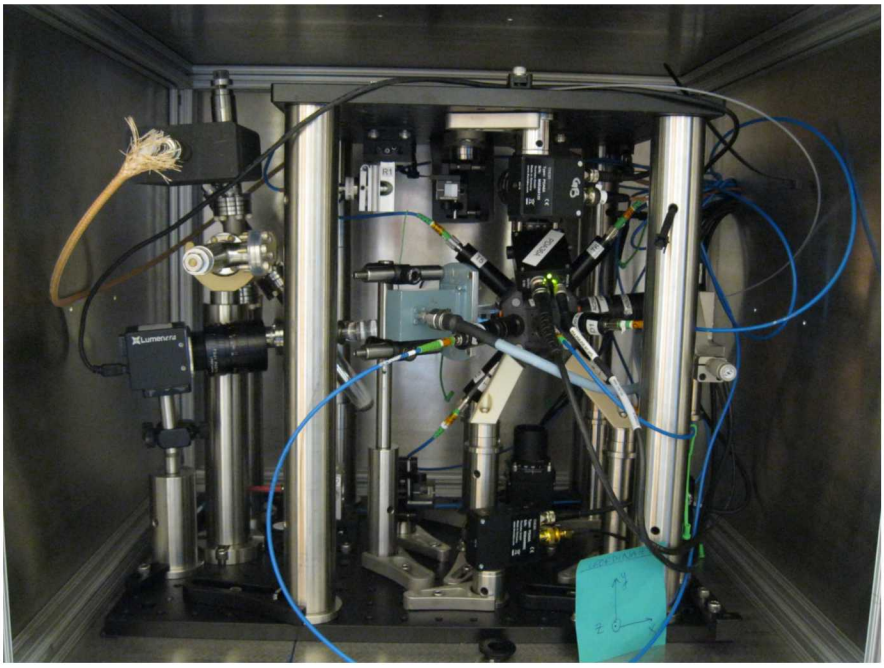

Figure 3.1: This photo shows the entire sensor head mounted inside the magnetic shield.

3.1 Vacuum

The experiment is conducted under vacuum in an all quartz cell connected through a metal glass transition to standard CF16 vacuum components. The original cell has been replaced by one with an AR coating at

780nm and the entire assembly has been tilted by 5 degrees from horizontal to prevent the formation of fringes in the vertical Raman beams. These spatial fringes would vary the Rabi frequency across the atom cloud and cause a significant reduction in contrast.

The vacuum is maintained by an ion pump holding a base pressure of 10^{-8}mBar. Our high-bandwidth scheme allows us to tolerate much higher background pressures than a typical experiment running at T times of 100ms. We load directly from room temperature rubidium vapour removing the need for complex differential pumping stages or oven based dispensers. Rubidium was introduced to the experiment with an ampoule isolated from the main vacuum with a valve, heating tape was used to drive rubidium into the experiment cell. Whilst background Rb vapour allows efficient MOT loading, even limited temperature control (with a peltier cooler) allows the vapour pressure at the MOT to be precisely adjusted. Rakholia used this to optimise the balance between recapture efficiency and loading rate; it is likely that we would also benefit.[19]

3.2 Optomechanical and magnetic Assembly

The optomechanical and magnetic assembly, consists of a frame machined from G10 (a fibreglass epoxy) from which almost all of the optical beams and coils are delivered to the experiment. The Raman beams are carried to the sensor head through two separate fibres, and delivered to the atoms through optics mounted directly to the plates above and below the vacuum cell. The frame itself is mounted directly over the glass cell with approximately 2mm clearance on each side. It is positioned on 3D printed legs of differing lengths to achieve the 5 degree tilt. These legs are bolted to standard 1" optics post, which are in turn mounted to the base plate breadboard. The entire assembly is placed inside a mu-metal shield which helps to reduce the effect of stray fields on the interferometer.

3.3 Optical Delivery

Laser beams are delivered to the sensor through optical fibres. These beams must then be aligned, correctly polarised, and collimated before the experiment can take place. We achieve all of these functions with this optomechanical frame.

The frame features 16 optical ports 14 of which are tapped to allow 1/2" lens tubes to screw on directly (not all of these ports are in use). The position and orientation of these holes was designed such that the beams would all overlap at the experiment centre, and were constructed precisely enough that no further

alignment was be required.

The 6 MOT beams are delivered to the experiment in fibre, and pass through a 1/2" lens tube (2" in length) containing a $\lambda/4$ plate to produce the correct circular polarisation. The beams are not collimated, and we rely on the natural divergence from the fibre output to produce sufficiently large MOT beams.[20] The repump beam is collimated and circularly polarised, using a lens in addition to a $\lambda/4$ plate. The D1 depump light is also collimated, and has a linear polarisation set to match the quantisation axis. The two detection beams are collimated and circularly polarised, again with optics inside two opposing 1/2" lens tubes. This assembly resulted in alignment sufficiently precise to generate a MOT, sub-Doppler cool, optically pump, and run our detection sequence. The stringent requirements of Raman beam alignment did not allow us to pursue this approach, Raman delivery was achieved with separate optomechanics described below.

3.3.1 Raman

The Raman delivery system was achieved using COTS[1] components. Fixed package fibre collimators[2] are mounted inside flexure mounts[3] on top of a 1D translation stage[4], providing 3 of the required 4 degrees of freedom. The beam passes through a Glan-Taylor polariser[5] to provide polarisation purity of at least 100000:1. A cube mounted gold-mirror[6] and $\lambda/4$ plate direct the light onto the atoms. The mirror-cube is mounted on an additional 1D translation stage, providing the final degree of freedom needed for arbitrary Raman beam pointing.

3.3.2 Magnetic Fields

In addition to it's function as an optomechanical frame, it also contains groves designed to house the quadrupole and 3 bias coils needed to generate a MOT. The coils were made from bondable magnet wire[7]. After winding onto 3D printed forms, they were cured at 200° for 30 minutes. The rigid coils were then simply slid into the corresponding groves in the optomechanical frame, and adhered with a small amount of epoxy. Tight grove tolerances ensure the coils are centred with respect to the cooling beams.

Placing the coils close to the vacuum chamber makes it possible to generate the required fields and gradients with much smaller coils, drawing less power, offering lower inductance, and allowing much faster

[1] Comercial Off the Shelf
[2] μLS: FC10-NIR1 $1/e^2$ diameter 5.5mm
[3] Siskiyou: IXF1.0a with IXF1.75mb
[4] Newport: DS40-X on B-2B
[5] Thorlabs: GT10-B
[6] CCM1-M01
[7] MWS, 25AWG, Heavy, Polyester coated

switching times. The use of G10 and an all glass vacuum cell was mandated by the need to prevent the formation of eddy currents. Lenz's law states that these induced currents act to oppose the change in magnetic field, making it very difficult to switch the B field quickly. This is particularly important in our high bandwidth scheme as even a 1ms increase in switching time would reduce our bandwidth by 9%. In addition to these active bias coils, the entire assembly is mounted within a mu-metal shield to help reduce the effect of stray static fields on the interferometer.

CHAPTER 4

LASER SYSTEMS

4.1 Overview

The laser systems are the backbone of any light pulse atom interferometer. We use lasers to cool the atoms and generate a MOT, sub-Doppler cool, generate interferometry pulses, and detect the state of the atoms. The systems employed and their performance figures are discussed in the following section. Specific product citations are for the purpose of clarification only and are not an endorsement by the author.

4.2 SHG

The light for the Raman system is generated by frequency doubling the output of a fibre laser and amplifier at 1560nm. This offers a narrower line width than an equivalent ECDL (External Cavity Diode Laser) and has the potential for providing very large amounts of power.

Our fibre-laser seed is supplied by NP Photonics Rock module operating at 1560nm.[2] The Raman system uses an IPG Photonics fibre amplifier[3] generating 32W at 1560nm. Our frequency doubling is achieved in a Periodically Poled Lithium Niobate crystal supplied by Covesion[4] temperature stabilised to $\pm 0.01^\circ$ in a Covesion oven.[5] A similar system was demonstrated by San et al.[21]. The new cooling system will operate with a lower power amplifier[6], providing 11W rather than 32W as the system requires far less power to operate.

[2]NP Photonics: Rock Module, 50mW, linewidth $<$ 3kHz, Frequency range $>$ 100GHz, and modulation facility.
[3]IPG Photonics: EAR-30k-C-LP-SF
[4]Covesion: PPLN:MSHG1550-1.0-40
[5]Covesion: PV40 Oven with OC2 temperature controller.
[6]IPG Photonics: EAR-30k-C-LP-SF

4.2.1 PPLN Mode Matching Theory

Boyd and Kleinman [22] demonstrated that the maximum conversion efficiency is achieved when the ratio of crystal length to confocal parameter is 2.84. This fixes the relationship between the diameter of the incoming beam D, the focal length of the coupling lens f, and the length of the crystal l.

$$b = \frac{l}{2\mathcal{R}} = 2.84 \tag{4.1}$$

As we begin with a collimated beam, we select the appropriate lens to give us the required Rayleigh range $\mathcal{R}$.

The diameter of a beam at its focal point is:

$$d_0 = \frac{4\lambda}{\pi}\left(\frac{f}{D}\right) \tag{4.2}$$

Where f is the focal length of the lens and D is the diameter of the collimated incoming beam. The Rayleigh range at the focus of a lens is:

$$\mathcal{R} = \frac{\pi d_0^2}{4\lambda} = \frac{4\lambda}{\pi}\left(\frac{f}{D}\right)^2 \tag{4.3}$$

Hence:

$$f = \sqrt{\frac{l\pi D^2}{22.72\lambda}} \tag{4.4}$$

For the Raman system $D = 1.1$mm, $l = 40$mm, and $\lambda = 1560$nm; giving an optimum focal length of 65.4mm. The closest available lens has a focal length of 60mm yielding $l/2\mathcal{R} = 3.38$. The cooling system amplifier has a slightly larger beam diameter $D = 1.2$mm; giving an optimum focal length of 71.5mm. The closest available lens has a 75mm focal length yielding $l/2\mathcal{R} = 2.58$.

4.2.2 Alignment

Aligning a free space frequency doubling system provided some unique challenges. SHG efficiency scales with input power squared making low power alignment impossible. The initial temperature was set based on Manufacturers data and coarse alignment was achieved by observing the crystal output on a silicon based CCD. Initially I optimised the input beam direction to generate a Gaussian output mode. The coupling was then optimised by maximising the conversion efficiency as measured on a silicon powermeter. Temperature

tuning was then achieved, with significant sensitivity to Crystal temperature observed down to the 0.05K level. Silicon detectors were used for measuring SHG output as they are completely blind to light at 1560nm and cannot mistake pump leakage for SHG. GaAs based detectors (including most IR powermeters) are particularly prone to this. With a higher sensitivity to photons at 1560nm than 780nm, even a small amount of pump leakage can dominate an SHG signal.

Due to the significant pump powers involved, I monitored the transmission efficiency of the crystal with a wavelength insensitive thermal sensor as pump power was gradually increased. A reduction in transmission efficiency would have indicated a potentially catastrophic heating. Even at 95% transmission efficiency, the local crystal heating by the pump beam was significant. The oven setpoint temperature was reduced from 81.2°C to 78.85°C to compensate for the local heating of 32W of pump power.

To reduce wavefront distortion, the doubled beam is collimated before passing through the filtering dichroic mirror[1]. As a result the collimating lens, (coated for 780nm) produced a powerful back-reflection in 1560nm, which at full pump power was several watts. To prevent damage to the crystal-oven a beam block was constructed from anodised aluminium with a very narrow central aperture, allowing the crystal output to pass but absorbing most of the diverging back-reflected 1560nm.

4.2.3 Green light

At pump powers above 15W green light became visible (see figure 4.1). This light is generated through 4-wave mixing, a nonlinear process coupling 3 photons at 1560nm and producing one at 520nm. The amounts of power are small, but as neither the eye protection nor the optics are coated for this wavelength these spots are visible and provided a useful check (through the use of back reflections) that the optics were aligned correctly.

4.2.4 Performance

The critical performance characteristics of a frequency doubling system are the maximum output power, and doubling efficiency. Measuring these quantities at such high beam powers is not entirely straightforward. The damage threshold of our power meter was ∼6W in a 1mm beam and both the input and output beams exceed this. For the pump beam we overcame this by using the indicated output power given by the amplifier itself, this was not always reliable and exhibited hysteresis and clear misreads. These misreads are the source of the vertically stacked points in figure 4.2. The output was measured with a thermal powermeter[2] and

[1] Thorlabs: DMSP1000, shortpass cutoff $\lambda = 1000$nm
[2] Thorlabs: S310C

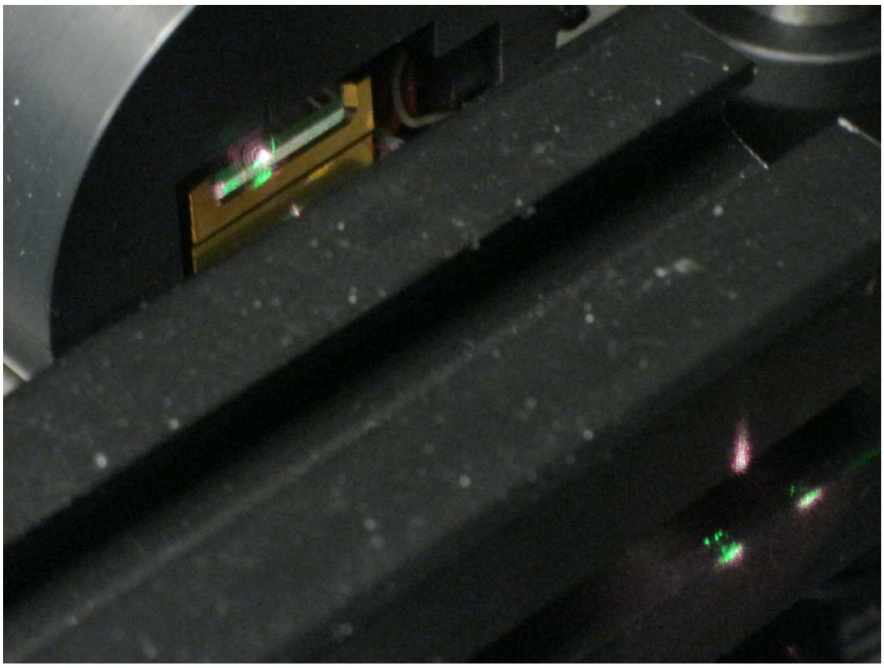

Figure 4.1: The green spots are caused by 4-wave mixing within the PPLN doubling crystal, the are visible on the crystal output facet (top left) and on the beam block after a back reflection from the collimating lenses.

these 'direct' measurements are plotted in figure 4.2 in magenta. The highest output powers exceeded the detector damage threshold so 'corrected' data was taken in which a PBS $\lambda/2$ pair attenuated the power to 39.1% before measurement. This factor was reapplied to the values before plotting the 'corrected' data in blue.

The fit in figure 4.2 only includes the corrected data series, the direct data is only shown to verify the correction. Equation 4.5 gives the result of this fit, showing a conversion efficiency of 0.967% per Watt. It also calculates that 2.5% of pump light reaches the sensor (consistent with the specs of the Dichroic mirror).

$$P_{780} = 9.67 \times 10^{-3}(P_{1560})^2 + 0.0254(P_{1560})\,\text{Watts} \tag{4.5}$$

The maximum output power was measured to be 12.0W. Given the uncertainty in the indicated pump power, I am confident that 12.0W is an accurate measurement of the power output of the system. The 9.9W measurement was taken with the pump set to 89% system power despite indicating 32.5W output, suggesting that this was an overestimate of pump power at that time. This conversion efficiency is almost identical to the 36% claimed by San et al. and our higher output power is due to a slightly more powerful amplifier.[21]

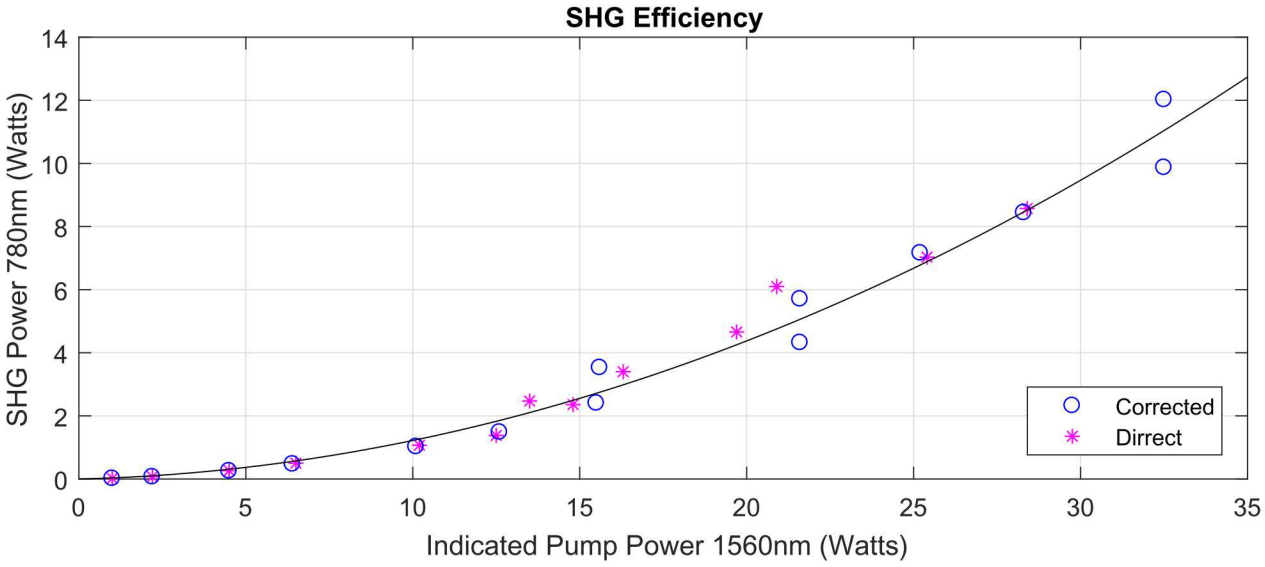

Figure 4.2: The SHG output is plotted against indicated pump power. The fit only includes the corrected data.

4.3 Raman System

The Raman system is required to produce two counterpropagating, orthogonally polarised beams, split by 6.8GHz, with common beam switching, and a fixed phase relationship at the atoms. Figure 4.3 shows the beam path used to generate the Raman beams. We generate up to 12W of 780 with SHG in a PPLN crystal. A beam sampler[1] diverts ∼1% of power to a fibre for frequency and sideband monitoring. The majority of the light passes through the common mode (COM) AOM which is used to switch both beams, controlling the pulse duration. The light is then split into two by a PBS (polarising beam splitter) and $\lambda/2$ plate to allow precise the control of the power balancing. Both paths go through an additional PBS (polarising beam splitter) and a half wave plate prior to fibre coupling. This allows the polarisation of the light to optimally matched on the PM fibre, minimising temperature and stress induced polarisation fluctuations, and subsequent power fluctuations on the atoms.

The 6.8GHz splitting is generated by modulating the 1560nm pump light with a fibre-EOM at 6.8GHz. Applying second harmonic generation (SHG) to a modulated source doubles the modulation depth but leaves the modulation frequency unchanged). Without further frequency manipulation, the combination of R1 and R2 would provide multiple valid pairs of Raman beams imparting momentum in both directions leading to at least two simultaneous interferometers. To prevent this we drive the EOM 74MHz blue of the 6.8GHz hyperfine splitting, and compensate the additional frequency shift with an AOM (OFFSET) in the R2 beam

[1] Newport: 10Q40NC.2

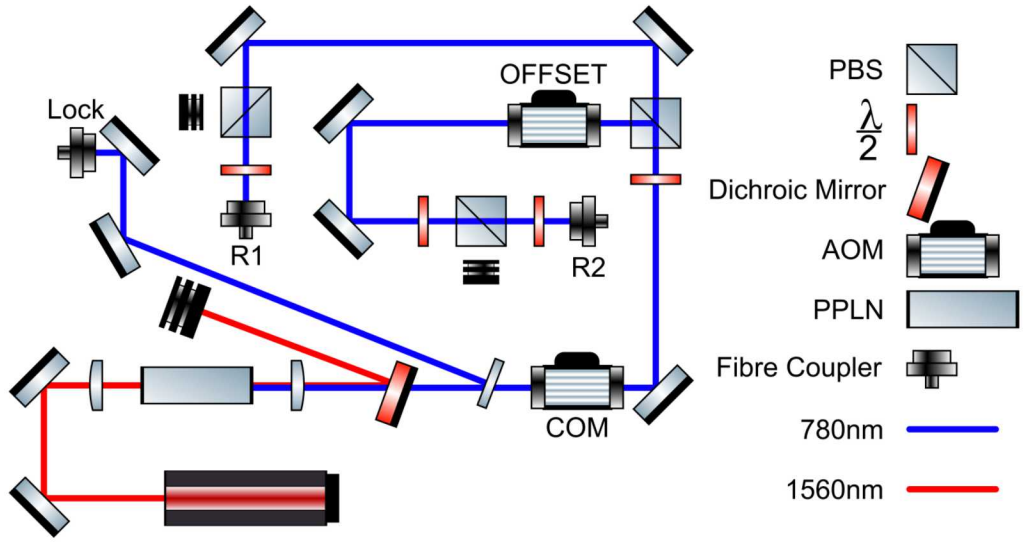

Figure 4.3: The above beam path shows the set up used to generate and stabilise the Raman beams. Frequency doubling is followed by an AOM network and three fibre outputs. The Raman beams (R1 and R2) are delivered directly to the atoms. The Lock output is monitored on a wavemeter and Fabry-Pérot. [23]

path. This ensures that only pairs of counterpropagating beams with a single $\mathbf{k}_{eff}$ match the frequency condition, removing the simultaneous interferometry problem.

If Doppler free Raman beams are desired, we use a single fibre to deliver both beams (blocking the unwanted fibre input) and remove the additional 74MHz EOM shift. The OFFSET AOM is not a problem in this case as it applies an equal frequency shift to both beams and simply increases the single-photon detuning Δ.

Due to very high AOM and fibre coupling efficiencies, this system can deliver up to 3.9W output from each of the two Raman fibres. This power is divided equally between the carrier and two side-bands. Only two of the three lines from each fibre can participate in the interferometer, forming two valid pairs with single-photon detunings Δ differing by the 6.8GHz hyperfine splitting.

4.3.1 Phase Lock

The OFFSET AOM can be used to phase lock the two Raman beams. By shifting the frequency of the AOM by δf for a small amount of time τ a phase shift $\delta f \tau$ can be added to that beam. The relative phase of the two beams could be monitored by combining a sample of the two Raman fibre outputs on a photodiode. The photodiode beat note (at ~6.8GHz) can be compared with a stable RF reference using an RF mixer or phase

detector generating an output proportional to any phase error. An appropriate PID loop fed back to the the AOM's RF input would remove any phase noise occurring before the beams are sampled. As optical phase noise induced by vibrations in the fibres is likely to be a dominant noise source in the interferometer, it is almost certain that a phase lock will be required.

4.4 Cooling and Detection System

The cooling system is required to generate 6 beams with at least 3mW of power, tunable from $\sim 10 \rightarrow 50$MHz red of the $F = 2 \rightarrow F' = 3$ transition (Rb^{87} D2 line, see A.1).[24] To use the same laser system for detection this tuning range must be extended to include resonance.

The current laser system for cooling and detection is based on an ECDL Master, tapered amplifier, and a set of AOMs. This system was in place before I began working on the project and has operated well in the past.[19] Due to a number of limitations and problems (discussed in the next section) we decided to replace the system. My completed designs are included here along with some expected performance figures. These will be implemented in future refinements.

4.4.1 Existing system

The following laser system was the one used to carry out all of the measurements included in this report. The seed laser is an ECDL, which after passing though optical isolators is fibre coupled. This light is delivered to the board shown in figure 4.4. This board splits the light with a PBS. An AOM shifts the frequency of the lock beam by 40MHz before delivering it to the lock components where the frequency is stabilised through Modulation Transfer Spectroscopy. The other beam traverses a double pass AOM centred on 150MHz and swept by $\pm$10MHz and is coupled into the output fibre. This allows us to scan the laser frequency by 300 ± 20MHz with an unwanted factor of 2 variation in output power.

The output from figure 4.4 is delivered to an injection-locked Slave laser and tampered amplifier (shown in figure 4.5). The injection-lock is there to smooth out the power variations caused by the Sub-D AOM and to amplify the power to the 30mW needed to seed the tapered amplifier. The 500mW TA output is fibre coupled and delivered to the AOM network described in section 4.4.3.

Whilst this system had operated well in the past [19], the Master laser diode's performance has degraded resulting in a reduced mode-hop free region at the required frequency and a resulting reduction in long term lock stability. The injection-lock and TA seeding are both inconsistent resulting in drifts in output power

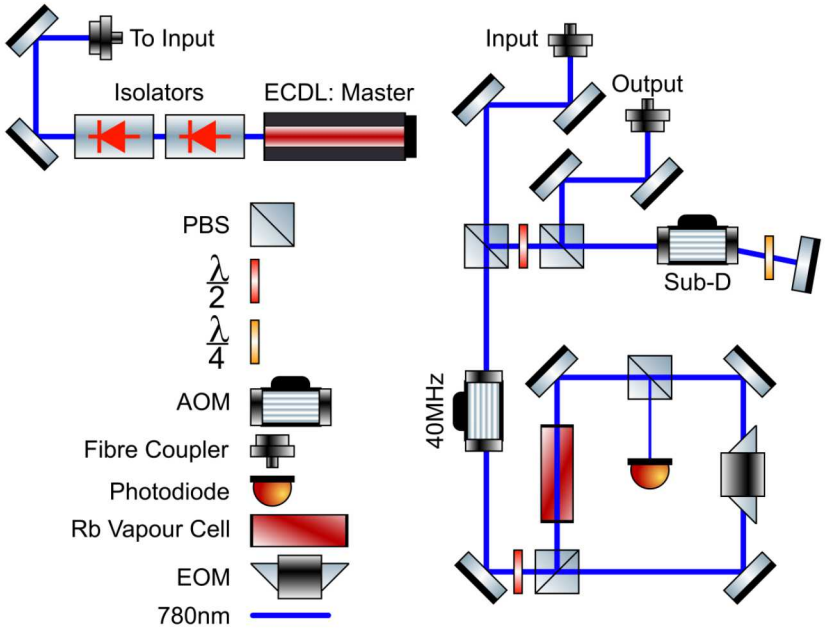

Figure 4.4: This beam diagram shows the ECDL seed (top left) and the board used to lock the laser and sweep the frequency for sub-Doppler cooling (right). The output from this board is delivered to the optical amplifiers shown in figure 4.5. [23]

requiring daily realignment. The system is exhibiting frequency noise from an unknown source at a level sufficient to degrade our measurement fidelity. The 500mW TA output limits our cooling beam power to (<5mW per beam), and we should achieve an increase in atom number with more cooling power. For these reasons it was decided that we would upgrade this system.

4.4.2 Upgraded system

The upgraded system (see figure 4.6) is based on frequency doubling of 1560nm analogously to the Raman. The fibre coupling efficiency from the TA was poor at only 30% resulting in less than 200mW of power delivered to the AOM network. A fibre based amplifier allows much higher coupling efficiencies ∼70%, so a large increase in usable power can be gained from only a modest increase in output. We chose an 11W fibre amplifier (10W specified) which we expect to generate 1.1W of 780nm and deliver 800mW to the AOM network. This should allow us to deliver cooling beams in excess of 20mW per beam without any further changes. The lock fibre will deliver ∼1mW of power to the spectroscopy board described in section 4.7.2.

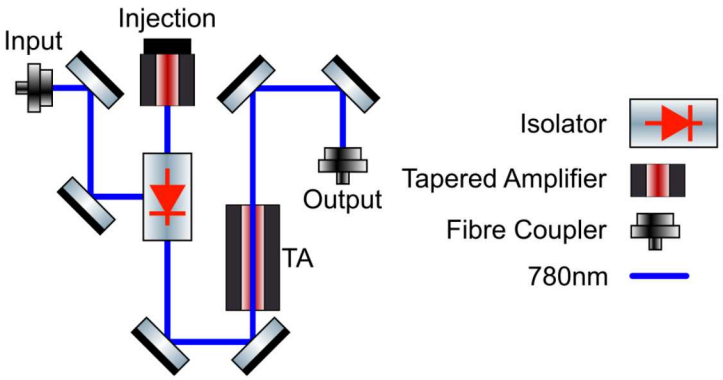

Figure 4.5: This is the amplification board in the existing laser system. The 1.5mW input seeds an injection-locked diode which in turn seeds the tapered amplifier generating 500mW of output for the AOM network.[23]

4.4.3 AOM Network

The AOM network is common to both the existing and upgraded laser systems. It splits the input light into 4 output channels and allows them to be switched individually. The power in each channel can be varied by adjusting a series of $\lambda/2$ plates. The switching is achieved with a double passed 80MHz AOM and the output fibre coupled. The RF used to drive these AOMs is switched with solid state switches triggered by a TTL input from the control system. The RF amplitude for C1 and C2 is adjusted with voltage control attenuators also driven by the control system. This allows precise control of both the timing and amplitude of these beams. This AOM network predates my involvement with the project and other than routine alignment is completely unchanged[19].

The outputs from this network are connected in the following way. C1 and C2 are both connected to in-fibre beam splitters, producing 4 and 2 outputs respectively. These fibres are connected to the lens tubes attached directly to the optomechanical frame described in chapter 3.3. The beams are allowed to freely expand, (passing through a $\lambda/4$ plate within the lens tube) and reaching a diameter of $\sim$10mm at the MOT and delivering 3.5mW per beam.

C4 is connected to an in-fibre splitter producing 2 outputs used for detection. These fibres are also connected to lens tubes on the optomechanical frame, but these tubes contain a lens to collimate the fibre output in addition to the Quarter wave plate. For the detection beams, it is particularly important that both the power and beam diameter are well controlled.

C3 is currently unused, but may in future be connected to a photodiode to allow us to monitor the system's output power and frequency. Combined with a MOT signal this would allow us to measure the

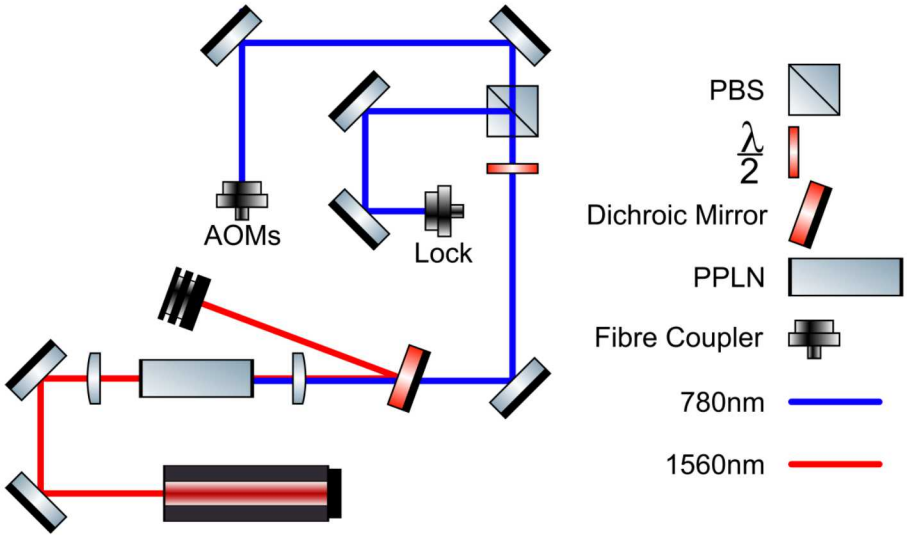

Figure 4.6: The setup used to generate and fibre couple the light for cooling and detection in the upgraded system. After frequency doubling the light is split and coupled into two fibres, one for frequency stabilisation, and the other to deliver light to the AOM network.[23]

MOT population on a shot by shot basis.

4.5 Depump Laser

The cooling and detection beams both address the $|F = 2\rangle \rightarrow |F' = 3\rangle$ transition on the D2 line of Rb^{87}. In order to prepare the atoms into our desired $|F = 2, m_f = 0\rangle$ ground state sublevel we use a π polarised laser resonant with the $|F = 2\rangle \rightarrow |F' = 2\rangle$ transition in the D1 manifold (see A.2). The $m_F = 0$ ground state is dark to this transition so applying it in parallel with our repump laser (section 4.6) results in efficient optical pumping to this state. The laser is a Vescent Photonics DBR (distributed Bragg Reflector) locked to the desired transition with a saturated spectroscopy module.[1] Ideally a single AOM would be used to switch the laser output, but the laser is locked to the desired output frequency so we require a second AOM with an equal and opposite frequency shift to maintain the resonance condition; beam path shown in figure 4.8. This system was designed and constructed by Adrian Orozco fellow PhD student.

[1] Vescent Photonics: Spectroscopy Module

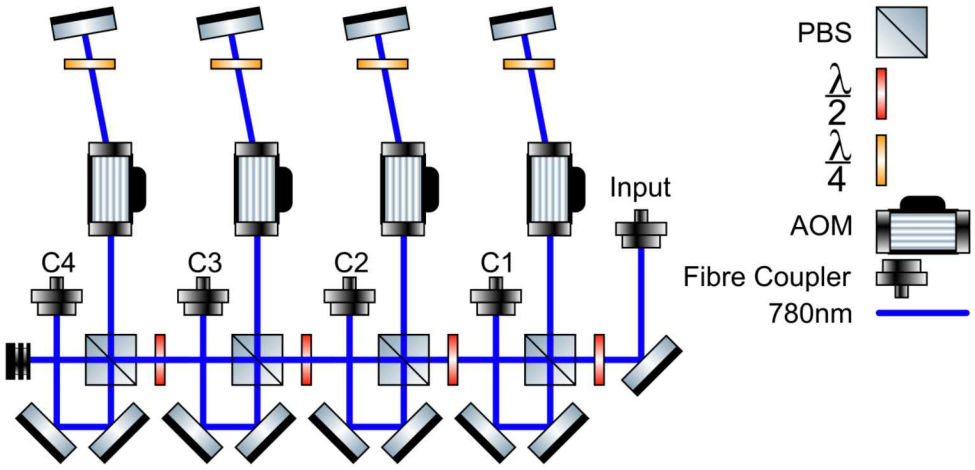

Figure 4.7: This is a schematic of the AOM network described in section 4.4.3.[23]

4.6 Repump Laser

The cooling transition in Rb^{87} ($|F = 2\rangle \rightarrow |F' = 3\rangle$ in the D2 manifold) is almost a closed cycling transition, but there is a small probability that the electron falls to the $|F = 1\rangle$ ground state and goes dark. To prevent this we employ the Repump laser resonant with the $|F = 1\rangle \rightarrow |F' = 2\rangle$ transition in the D2 manifold. This repumps population from the dark state and allows both efficient cooling and total population detection to occur. This laser is based on another DFB diode locked through Modulation transfer spectroscopy to a Rb vapour cell. It is switched with a single AOM operating at the frequency required to achieve resonance. As with our other systems pulse duration is controlled through the use of solid state switches in the AOM RF lines, which are in turn driven by TTL channels from the control system.

4.7 Laser frequency Control

4.7.1 Raman

For the Raman beams common mode frequency noise will change the single-photon detuning (Δ) which will in turn change the Rabi frequency (see chapter 2). This causes fluctuations in the fidelity of the matter-wave optics, reducing fringe visibility (see figure 2.2). Whilst this can reduce contrast, for large detunings $\Delta > 1$GHz the passive stability of the seed laser is sufficient to prevent significant reductions. We monitor the frequency with a wavemeter offering ~100MHz accuracy which is sufficient for setting a detuning. We also monitor the relative sideband powers with a Fabry-Pérot. Sideband asymmetry is corrected by temperature

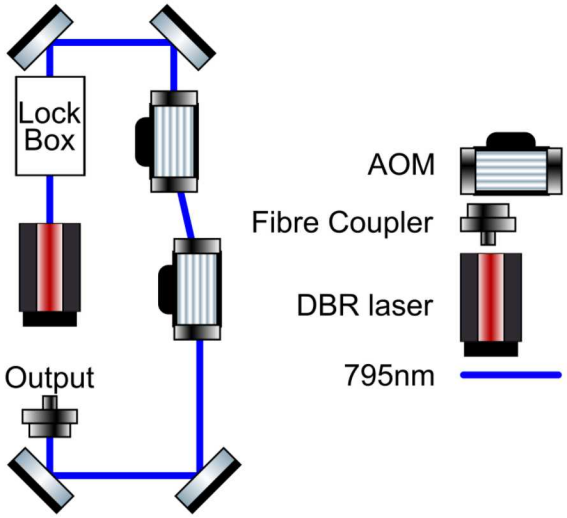

Figure 4.8: This is the beam path used to generate, lock and switch the Depump light. Designed and constructed by fellow PhD student Adrian Orozco.[23]

tuning the PPLN crystal; they are found these to have passive long term stability once balanced. The most important specification in the Raman system is the frequency of the sidebands; but fortunately this is controlled by commercial RF components electronics with ∼1Hz level stability and is not a measurable source of noise in this system.

4.7.2 Cooling and Detection

For our detection system to perform at the atom shot noise limit it must have a frequency variation between the two detection pulses of less than ∼10kHz. Frequency variation between these pulses will change the amplitude of the signal, giving us noise indistinguishable from phase noise in our interferometry fringes. It was exactly this problem that motivated the design of the upgraded system.

The existing Cooling and Detection laser described in section 4.4.1 is locked to a rubidium vapour vapour cell using modulation transfer spectroscopy with feedback on the diode current (beam path shown in figure 4.4). The new system will operate with a DFB fibre laser master exhibiting a narrower intrinsic linewidth and better passive stability reducing the demands on the lock servo. It eliminates all but one of the original AOMs removing several potential sources of frequency noise and severe sources of amplitude noise. One AOM per path is still required in the switching network. The removal of these AOMs also eliminates 360MHz of required frequency shift and the ability to sweep the laser frequency (required for sub-Doppler cooling).

We use modulation transfer spectroscopy of rubidium vapour (see figure 4.9) to lock the laser to the

$F = 3 \rightarrow F' = 4$ transition on the D2 line of Rb^{85} with light delivered in fibre from figure 4.6 (lock fibre).[25][24] This lock point is 1.1GHz Blue detuned from the desired $F = 2 \rightarrow F' = 3$ D2 line in Rb^{87} and 50MHz further still from the required final frequency for sub-Doppler cooling. To generate this frequency shift and retain the sweep functionality we modulate the incoming light with an fibre-EOM at 966.49MHz to 1016.49MHz. The RF for this is supplied by a DDS[1]. The light is spectrally filtered by a temperature stabilised Fabry-Pérot such that only the blue sideband is present in the spectroscopy cell. A polarising beam splitter (PBS) and a half wave plate ($\lambda/2$) are use to divide the beam into a low power probe, travelling straight through the cell, and a high power pump beam. The pump is modulated by a freespace EOM before counterpropagating through the vapour cell in a path that overlaps with the probe. The probe beam is directed onto a photodiode, where an error signal can be generated with standard RF electronics. A PID controller takes the error signal and feeds back to the laser current closing the loop.

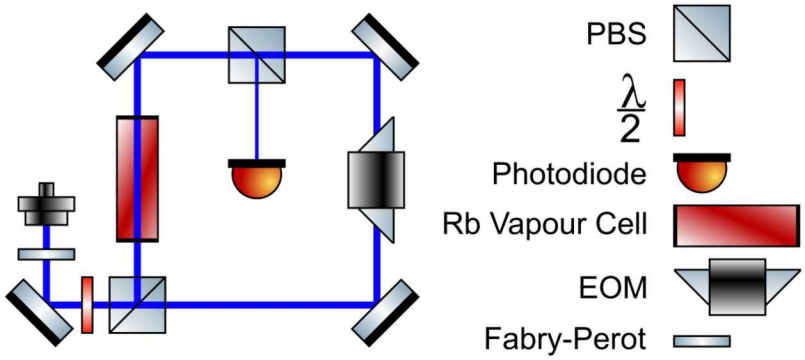

Figure 4.9: This is the beam path used to implement Modulation Transfer Spectroscopy in the upgraded system. It is near identical to that used in the existing system with the notable addition of the Fabry-Pérot.[23]

[1] Analog Devices: AD9914

CHAPTER 5

LASER COOLING AND THE MAGNETO OPTICAL TRAP

The following section outlines the theory and practical details of our MOT and cooling procedure and systems.

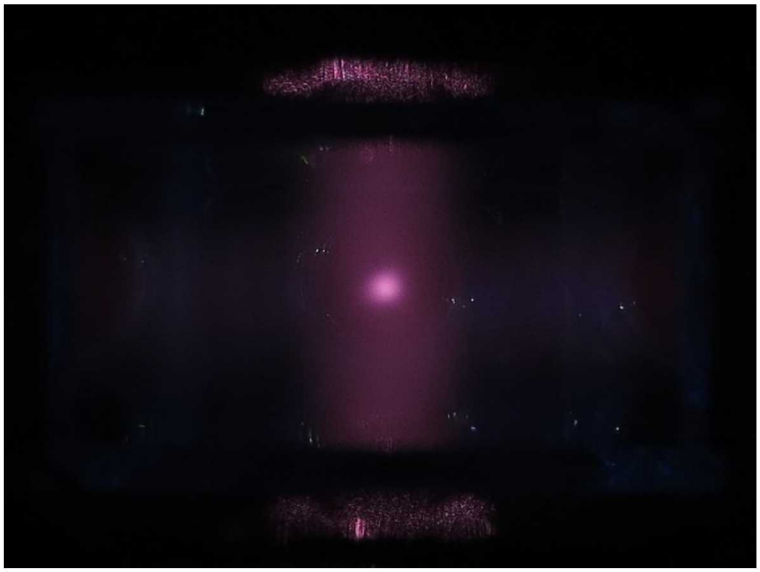

Figure 5.1: This is a long exposure photograph of our Magneto Optical Trap (MOT). The cooling beams can be viewed passing through rubidium vapour in the cell.

5.1 Theory

Laser cooling and trapping relies on the ability to exert a controllable force on an atoms with laser light. A careful combination of laser beams and magnetic field gradients act together to cool and confine atoms into a low temperature cloud confined to $\sim$1mm^3 . Laser cooling and trapping have been described in excruciating

detail by numerous papers and every cold atom thesis since 1990; for additional information the following references provide canonical, early, or particularly instructive explanations.[26][27][28][29][30][31]

I will tackle the problem in two parts, first describing how the interaction between an atom and a laser beam can result in cooling. Secondly I will introduce a magnetic field gradient and explain why this can result in spatial confinement.

5.1.1 Laser Cooling

A photon carries momentum $\mathbf{p} = \hbar\mathbf{k}$. When an atom absorbs a photon, the atom recoils with equal momentum. The atom, now in an excited state will emit a photon in a random direction, causing an equal and opposite atomic recoil. The spontaneous emission occurs in a random direction, so over many scattering events the effect of the spontaneous photons on the atom's momentum average to zero. This approximation of a large number of scattering events is valid, with $\sim 10^3$ photons needed to cool an atom of Rb^{87} from it's capture velocity of $4ms^{-1}$ (corresponding to a temperature of $T = 0.2K$) to base temperatures of $\sim 100\mu K$. It is interesting to note that only the coldest atoms in the Maxwell-Boltzmann distribution are travelling slowly enough to be addressed by laser cooling.

To turn this momentum transfer into a cooling process it must be velocity dependant. We achieve this with the Doppler effect. By operating the laser at a frequency $\sim$10MHz below resonance (red detuned) we ensure that only atoms with a velocity component directed towards the laser beam are able to absorb photons and be cooled. When this velocity component vanishes no further recoil events can occur. As the initial velocity of the atoms is unknown we require cooling in both directions for all 3 spatial dimensions. We achieve this with 6 counter propagating beams, although systems can function with as few as four.[32]

There are several limits that apply to the base temperatures achievable with these processes. The minimum temperature that can be conceived of with discrete $\hbar\mathbf{k}$ photon momentum kicks is the temperature at which an additional scattering event raises the temperature of the atom (known as the recoil limit). For Rb^{87} this is 361.96nK.[24] This is the lowest temperature theoretically achievable with laser cooling.

Unfortunately this temperature is not achievable with the cooling procedure described above. At sufficiently low temperatures the spontaneous emission, whilst still satisfying $\langle v \rangle = 0$, causes the atoms to undergo a random walk $\langle v^2 \rangle \neq 0$. This random walk has an associated kinetic energy, which with optimum trapping parameters corresponds a minimum temperature $T_D = \frac{\hbar\Gamma}{2k_B}$. This is known as the Doppler temperature and for Rb^{87} is $145.57\mu K$.[24]

We are able to beat this temperature with sub-Doppler cooling processes. Polarisation gradient cooling

allows us to reach a temperature of 11μK, with temperatures as low as 2.5μK demonstrated elsewhere.[33] PG cooling is achieved by removing the quadrupole field whilst simultaneously red-detuning the cooling lasers and reducing the intensity. We sweep the frequency from 10 $\rightarrow$ 50MHz red of the cooling transition whilst reducing the intensity to 0 over 1ms. A detailed description of polarisation gradient cooling can be found in *Laser Cooling and Trapping* by Metcalf and Straten.[30]

5.1.2 Magneto-Optical Trapping

The processes described above cools atoms within the region of space in which the beams overlap, but does not provide any trapping. Laser cooling on it's own is a viscous damping process with a non-zero $\langle v^2 \rangle$ (this is commonly known as optical molasses after the damping effect experienced by an object moving through treacle). This does provide an increase in density proportional to the cube of the velocity reduction ratio.

We desire much higher atom numbers and more importantly densities for our interferometer. We achieve this by applying a magnetic field gradient across the beam overlap region. This gradient Zeeman shifts the magnetically sensitive $m = \pm 1$ sub-levels by an amount proportional to the distance to the magnetic field null. The correct choice of cooling beam polarisations ensures that a cold atom moving away from the field null is brought onto resonance of the red-detuned beam with $\mathbf{k}$ directed back towards trap centre. Adding this spatially varying confinement force on top of the viscous damping generated by the molasses results in a dense cold cloud of atoms at the magnetic null. This is a magneto optical trap (MOT). Figure 5.2 is an illustrated example of an atom moving within a MOT.

5.2 Experimental Realisation

We generate our MOT and implement sub-Doppler cooling with the apparatus described in chapter 3.3, but in summary it consists of 6 counterpropagating beams within a quadrupole field. The beams freely expand from fibres with only the addition of $\lambda/4$ plates to generate the correct polarisation.[34] Each beam carries 3.5mW of power and at the trap centre is 10mm in diameter. The quadrupole coils are set up in the anti-Helmhotz configuration with 50 turns per coil, each turn being a square 24mm $\times$ 24mm. At 2A operating current they generate a field gradient of 9 Gauss/cm at the trap centre. The original quadrupole coils were larger and had fewer turns, but due to a dimensional asymmetry produced a highly asymmetric MOT, shown on the left of figure 5.3. Whilst this 'cigar' shaped MOT (aspect ratio $\sim$5:1) may prove to be a very efficient way to load an atom guide, for our present experiment it is inconvenient.[35][36][37][38][39] The new square

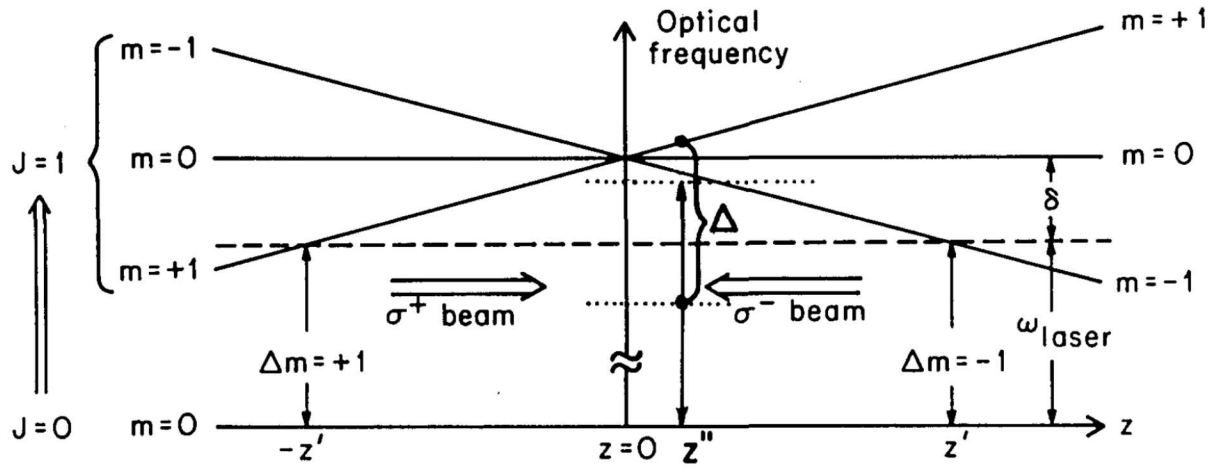

Figure 5.2: Arrangement for a MOT. The horizontal dashed line represents the laser frequency seen by an atom at rest, and the two shorter dotted lines represent the frequencies of the opposing laser beams seen by a moving atom. At $z = z''$ an atom moving to the right sees the σ^+ beam detuned by Δ, but the σ^- beam is almost resonant with the transition to $m = -1$. This diagram was taken from reference [31].

coils generated the much rounder MOT shown on the right of figure 5.3. The axial profiles of both MOTs were near identical with an end on view of the new MOT shown in figure 5.4. The critical properties of any cold atom source are its atom number and temperature. These are discussed in the following section.

5.3 Performance

5.3.1 Atom Number

We measure the atom number by observing the fluorescence of an illuminated atomic cloud on a photodiode[1]. The relevant atom number for interferometry is that observed during an interferometry cycle, is generally lower than the steady state value because the MOT loading time restricted. The scattering rate per atom is given by:

$$R_{sc} = \left(\frac{\Gamma}{2}\right) \frac{(I/I_{sat})}{1 + (I/I_{sat}) + (2\Delta/\Gamma)^2} \tag{5.1}$$

Where Γ is the excited state lifetime, I is the intensity of the incident Radiation, I_{sat} is the saturation intensity, and Δ is the detuning measured in radians. The saturation intensity is a property of the atomic transition and is in general dependant on the polarisation of the light. The derivation of this formula and a

[1] Thorlabs PDA36A with gain at 70dB

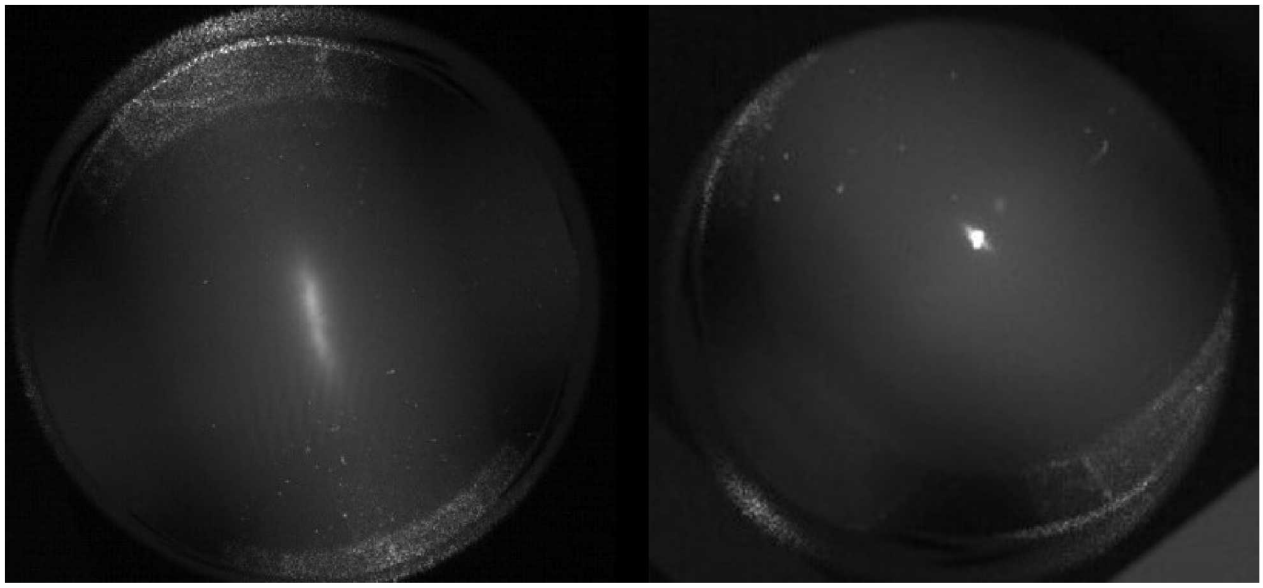

Figure 5.3: The left photo is a plan view of the original MOT, the asymmetric ∼5:1 shape is caused by a 2:1 aspect ratio in the quadrupole coils. The new MOT is shown on the right. Utilising square quadrupole coils we were able to generate a far more rotationally symmetric MOT.

discussion of the approximations involved can be found in Steck Rb^{87} Line Data.[24]

The detection beams are collimated, σ-polarised, counter propagating beams and as such their scattering rate can be simply calculated allowing an accurate determination of atom number. The beam diameter is 4.5mm, with 500μW per beam.

For a 25ms cycle and a 2ms freefall (i.e MOT loading for 21ms per cycle) we observe a steady state atom number of 1.2×10^7. For a 25ms cycle and a 7.5ms freefall (i.e MOT loading for 15.5ms per cycle) we observe a steady state population of 5.1×10^6. The difference is due to a reduced loading time per cycle. With optimisation of the MOT parameters the recapture efficiency should be increased resulting in a higher steady state atom population. Rakholia et al. demonstrate 86% recapture efficiencies in an interferometer operating with a 20ms cycle time.[12]

Our observed atom number of 1.2×10^7 appears to be low for 10mm cooling beams with an expectation of 10^8 atoms.[40] This may have a number of causes. The measurement underestimates the population that would result from continuous cooling. It was taken after both sub-Doppler cooling and optical pumping had occurred, which could result in some loss. Our experiment would benefit from increased optical power in the cooling beams, $I/I_{sat} = 15$ compared to 108 in a similar experiment by McGuinness.[41] These errors can be addressed and should result in a larger atom numbers, and a more predictable system.

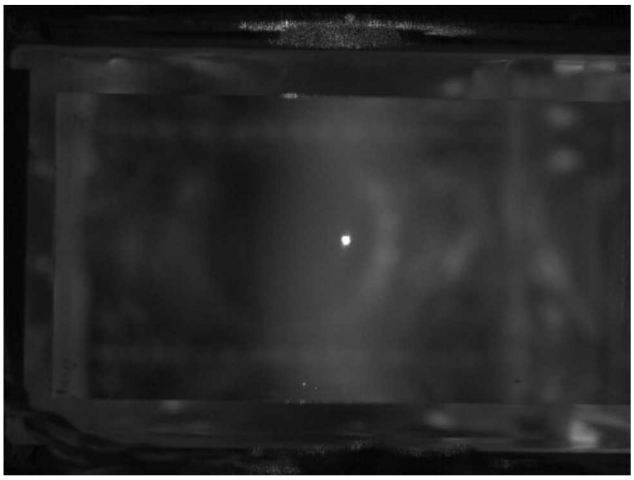

Figure 5.4: This is an end on view of the new MOT. This is very similar to the end on view of the original MOT. Under normal circumstances the collection optics for detection are mounted in the location of this camera.

5.3.2 Temperature

In chapter 7.5 we exploit the Doppler sensitive nature of our Raman beams to measure the temperature of our sub-Doppler cooled atom source. We observe a temperature of $T_a = 10.9\mu$K. This is above reported temperatures for similar high-bandwidth experiments ($T_a = 5.5\mu$K)[41], and well above the 2.5μK achieved in low-bandwidth experiments.[33] Optimisation of the intensity and frequency ramps during sub-Doppler cooling can improve this temperature. In any case, our short T time makes us far more tolerant of high cloud temperatures than typical $T = 100$ms experiments.

CHAPTER 6

EXPERIMENTAL SEQUENCE

The following section details the experimental sequence used for atom interferometry including the timing for specific sections. Most of this information is presented in more detail elsewhere in the document.

6.1 Timing

The following section considers a single experimental cycle with emphasis on the relative timings and durations of each event. Figure 6.1 is a summary of the entire sequence.

6.1.1 Cooling

We begin the sequence with a MOT already loaded into the trap, with the MOT coils, cooling, and repump beams remaining on unless an experiment is in progress. 70μs into the sequence the polarisation gradient cooling begins. The quadrupole coils are switched off (taking $\sim$100μs). In parallel with this, the cooling beams are swept in frequency from 10 $\rightarrow$ 50MHz red detuned and the intensity is attenuated to 0 over 1.5ms.

6.1.2 Optical Pumping

1.57ms into the experiment we introduce a bias field to define a quantisation axis for the optical pumping light. We wait 10μs for it to switch on and then start the Depump beam. After 200μs the optical pumping is complete and we switch off first the Depump beam, and 10μs later the repump beam (this delay ensures that all the atoms are initialised into $F = 2$). In addition to switching the repump beam, we also rotate the bias field to match the quantisation direction of the Raman beams in preparation for interferometry (vertical rather than the 5° tilt required for the optical pumping). We are now at 1.79ms

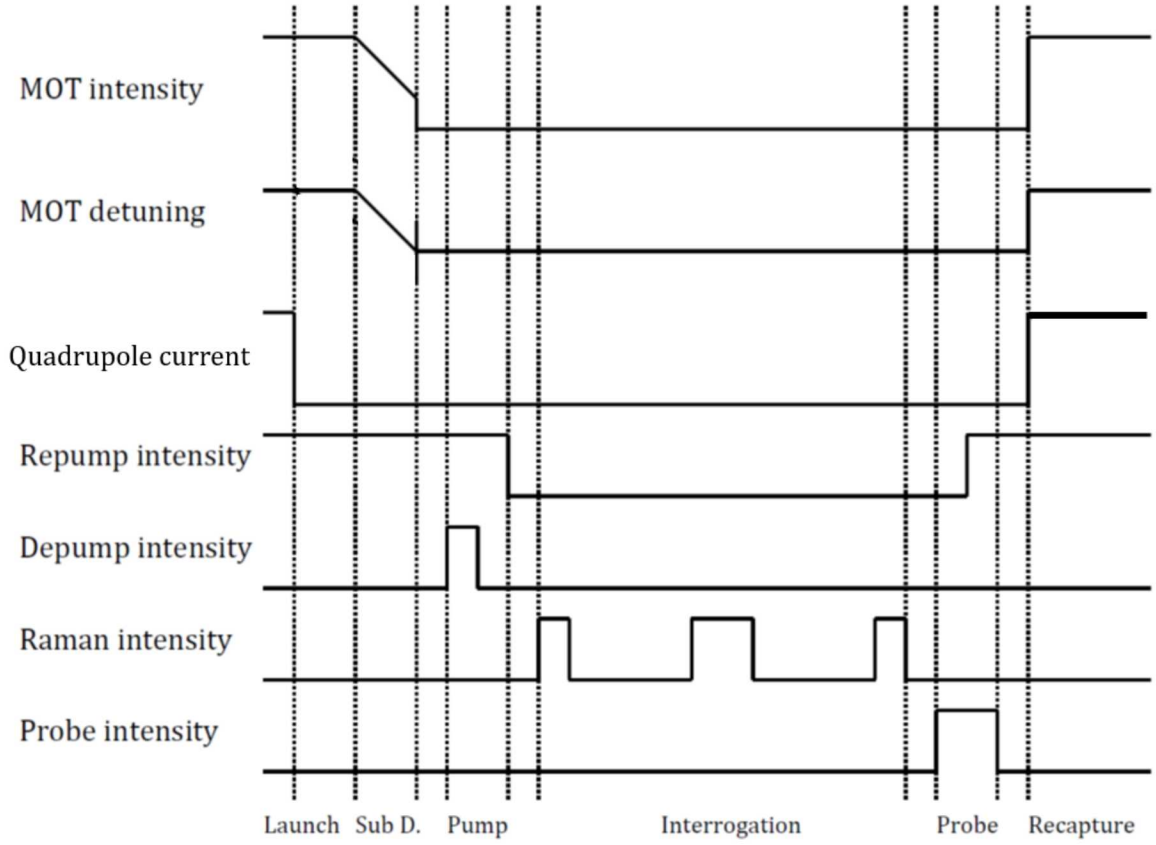

Figure 6.1: This diagram shows the timing of key events in the experiment (not to scale). The full experiment duration is approximately 25ms. This diagram was taken from the PhD thesis by A. Rakholia [19] and modified.

6.1.3 Interferometry

We now wait for 300μs to ensure that the magnetic fields have time to reach their steady state values and completely stabilise. At 2.09ms we trigger the FPGA, which controls the duration and timing of the Raman pulses. This is when the atom interferometry takes place. The duration if this freefall was varied with the desired interrogation time, but at it's longest it was 10ms. We typical used the shorter freefall time of ~7ms. In the typical case 9.09ms has elapsed since the start of the cycle, but for different experimental parameters this varied from 4ms up to longer than 12ms. Once the experiment is fully optimised, still longer interferometry times may yield the highest sensitivity. Hence forth I will assume the typical case was used.

6.1.4 Detection

With the interferometry pulses complete and the atoms still in freefall the magnetic fields are adjusted to rotate the quantisation axis into alignment with the detection beams. We switch the coils 10μs before switching on the detection beam. The detection fields were never optimised and after careful optimisation it is likely that a longer delay time will increase detection stability.

The detection beams start 9.1ms after the start of the cycle. We wait for an additional 40μs before recording the atomic florescence with an APD (avalanche photodiode). The additional delay reduces our sensitivity to AOM rise time, and allows additional time for the magnetic fields to stabilise. We record florescence between 9.14ms and 9.2ms at which point we start the repump beam. This introduces the $F = 1$ population into the detection loop and allows us to normalise against fluctuations in atom number. We allow another 40μs delay before recording florescence for 60μs. Taking the ratio of the two signals (after subtraction of backgrounds) and applying a simple scale factor yields the atom probability $P(F = 2)$. The detection sequence is complete at 9.3ms.

6.1.5 Recapture and loading

With the experiment complete we restart the cooling beams, repump, and quadrupole coils. This recaptures the majority of the atoms and then continues to load the MOT from background vapour. The experimental control system currently operates a fixed cycle time of 25ms. In the typical case described above the MOT recapture and loading is allowed to run for 15.7ms, but this time will vary with the chosen freefall time. This loading time is one of the parameters that will need to be adjusted to realise the maximum experimental performance. Several capture times, and the corresponding atoms numbers are described in chapter 5.3.1.

CHAPTER 7

ATOM INTERFEROMETRY

The following section contains a characterisation of the atom interferometer. We first consider the efficacy of our optical pumping with a microwave π-pulse, and the use of this technique for measuring and cancelling stray magnetic fields. We consider Doppler-free Raman pulses and their efficiencies as a further validation of this measurement and of our Raman beam alignment. We combine Doppler sensitive Raman pulses in a Ramsey sequence to demonstrate an atom interferometer and measure the projection of $\mathbf{g}$ along the Raman beam axis; approximately $\mathbf{g}$. We exploit the Doppler sensitivity of the Raman pulses to measure the temperature of the sub-Doppler cooled atomic sample. Finally we consider how our powerful Raman beams can be used to enhance sensitivity.

7.1 Optical Pumping

The depump laser initialises the atoms into the $|F = 2, m_F = 0\rangle$ sublevel. We verify that this is successful with a scan in frequency of a π pulse delivered by a microwave horn, shown in figure 7.1. The microwave frequency is scanned about its resonance at 6.83468GHz. The pulse length is adjusted to realise a π pulse at 0 detuning, and this pulse length is used for the entire spectroscopy measurement. At larger microwave detunings the difference in π pulse length will reduce the transfer efficiency but that is not a significant effect here. Each data point represents a separate experiment comprising cooling, optical pumping, microwaves, and detection. The $m_f = 0 \rightarrow 0$ transition (located at 0 detuning) transfers 93% of the population from the $F = 2$ state. This means that at least 93% of the atoms must be initialised into this state, greatly exceeding the 20% expected from a randomly distributed sample. The transitions at $\pm$0.186MHz correspond to $m_f = 0 \rightarrow \pm 1$ and occur because the polarisation of the microwaves is not purely π. The peaks at $\pm$0.372MHz correspond to $m_f = -1 \rightarrow -1$ and $m_f = 1 \rightarrow 1$; both transitions show 3% transfer indicating

that 3% of the atoms are in each of these states. This is consistent with the optical pumping efficiency determined from the $m_f = 0 \rightarrow 0$ transition.

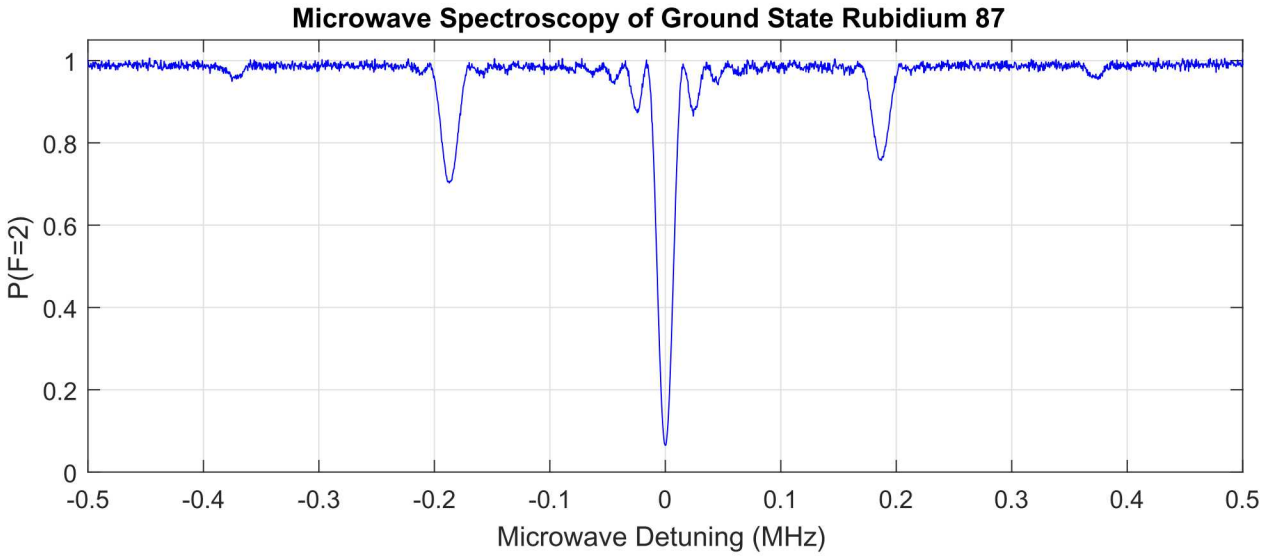

Figure 7.1: This plot shows the probability of finding an atom in the $F = 2$ ground state of Rb^{87} after the application of a microwave π-pulse. The microwave frequency is scanned around resonance at 6.83468GHz. The 93% transfer efficiency on resonance indicates that optical pumping is working efficiently.

The magnetic field applied to the experiment during this spectroscopy can be easily determined from the spacing of these peaks. The Zeeman sensitivity of these levels is 0.7MHz/G, therefore the magnetic field applied during this microwave interferometry is 0.265 Gauss. For optical pumping to succeed it is essential that a bias field is applied to set a quantisation axis for the atoms, and in turn ensure that the $|F = 2, m_F = 0\rangle$ sublevel is dark. When optimising the bias fields to cancel any background, RF spectroscopy can be employed in an identical way. A spectroscopy measurement is taken, the splitting measured, the current supplied to a bias field varied and the spectroscopy repeated. A reduction in peak spacing means that the residual fields has decreased, and vice versa. By iterating through the coils, it is possible to reduce the residual field to the point where all the Zeeman sublevels occur are degenerate, at which point the background fields have been nulled.

7.2 Doppler Free Raman Pulses

High bandwidth operation is difficult to achieve with Raman beam retroreflection. For retroreflection to succeed the atoms must be at sufficient velocity for the Doppler effect to discriminate between the original and reflected beams. In practice this means that the Doppler shift must be at least as large than the linewidth

of the Raman transition. For a Raman pulse length $t_\pi = 8\mu$s this condition is achieved after 9ms of freefall. This limits the bandwidth to 111Hz without allowing any time for atom loading or interrogation. In the 25ms cycle time we ultimately use this delay would reduce our bandwidth by 36% without considering the reduction in recapture efficiency caused by the increased freefall distance. Using shorter t_π times to address a larger velocity class of atoms (one of the key advantages of high bandwidth interferometry) would cause this free-fall delay to increase. Future experiments may use a launch to break the Doppler symmetry more quickly, but in our case we choose to avoid the experimental complexity and instead deliver our Raman beams through two separate fibres.

When setting up the experiment we initially operate in Doppler free mode where both beams are delivered by the same fibre and copropagate. Whilst this mode is not sensitive to accelerations it greatly simplifies the original alignment. The copropagating beams must only overlap with the atoms (by maximising Rabi frequency) and be parallel with vertical (though retroreflection from a horizontal mirror). With the first beam aligned in this way, we align the second by coupling it into the first's output port. This guarantees beam overlap, and provided the first beam was well aligned, verticality and atomic alignment. With the Raman beam aligned, we are able to proceed to the Doppler sensitive counterpropagating case.

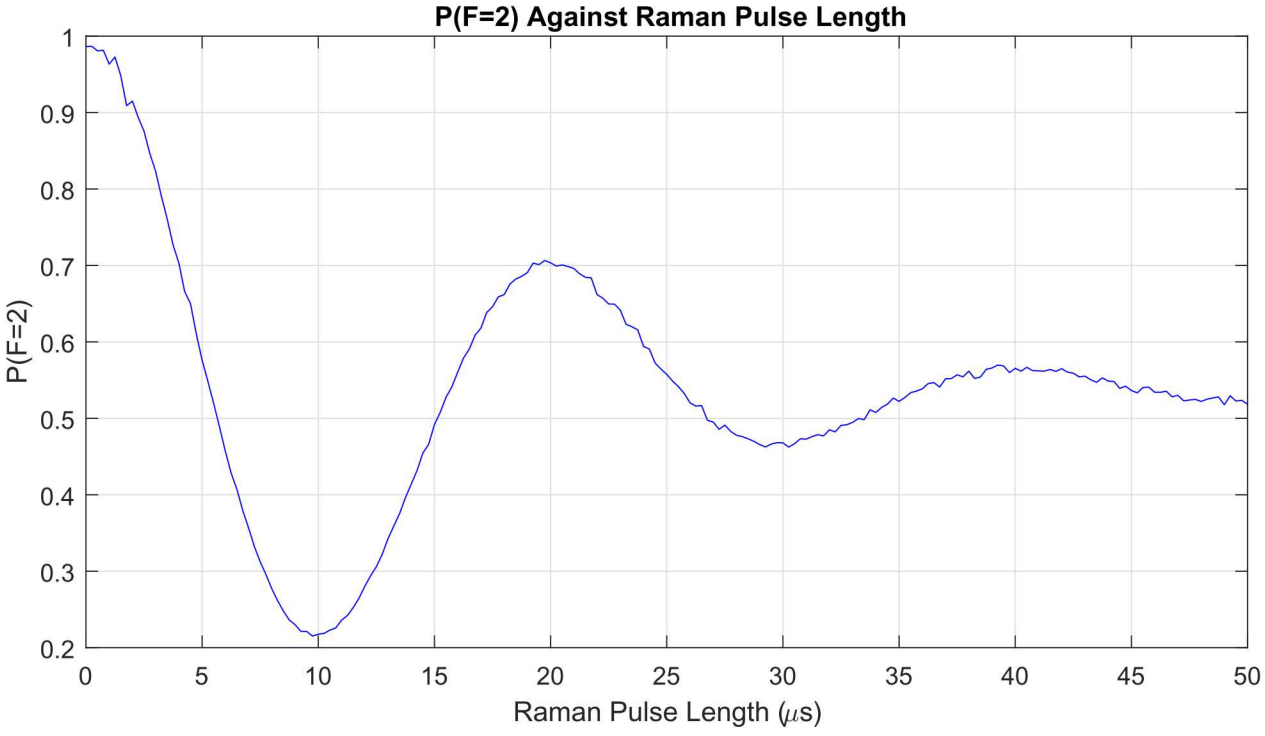

Figure 7.2: Doppler-free Rabi flopping with a Rabi frequency of 20KHz. The π-pulse efficiency is 78% providing further confirmation of successful optical pumping.

7.3 Doppler Sensitive Raman Pulses

To align the second Raman beam we adjust the delivery optics to couple the first beam into the second fibre. This through-coupling guarantees beam overlap, counter-propagation, atom overlap, and verticality (provided these conditions were met by the first beam). The fact that our Raman beams are 5.5mm in diameter relaxes the constraints on beam overlap and atomic alignment whilst still maintaining pulse efficiency. The coherence time and transfer efficiencies are both lower, for our Doppler sensitive beams likely due to the velocity selection caused by finite cloud temperature; discussed in section 7.5.

7.4 Atom Interferometry

Implementing a $\frac{\pi}{2} \rightarrow \pi \rightarrow \frac{\pi}{2}$ Ramsey sequence yields interferometry fringes. By measuring a large number of interferometers of increasing interrogation time T (spacing between pulses) we are able to generate a single plot that encompasses all of the key information about the interferometer, see figure 7.3. The interferometer phase increases quadratically with time $\Phi = -\mathbf{k_{eff}} \cdot \mathbf{g}T^2$. Including the effect of finite pulse durations on the accelerating atoms, we find the probability of measuring an atom in a given state to be: [42](corrected)

$$P_{|F=2\rangle} = \frac{1}{2}(1 - \cos(\Delta\phi)) \tag{7.1}$$

$$\Delta\phi = -\mathbf{k_{eff}} \cdot \mathbf{g}\left[T^2 + t_\pi\left(1 + \frac{2}{\pi}\right)T\right] \tag{7.2}$$

Figure 7.3A shows a scan of interrogation time T and exhibits both decreasing contrast at longer T-time and a shift in the mean value. Plot A shows the unprocessed data and the 1400 point moving average employed to remove the mean value drift. Plot B shows the data after subtraction of this moving average with a fit of functional form described in equation 7.2. Plot C shows the residuals of plot B. It is clear from these plots that for small T, sampling and periodicity mismatches cause oscillations in the moving average, effectively damping the scan for small values of T. More careful processing would vary the sampling length with T to remove this artefact. It is also clear that the amplitude decay rate has not been successfully matched. As we are primarily interested in the accumulation of phase, these errors are small, and do not result in a dropped fringe up to $T > 3500$, the fit in plot B is sufficient to determine $\mathbf{g} \cdot \mathbf{k_{eff}}$.

As figure 7.3B encompasses such a large number of oscillations, I have included reduced range sections to highlight the main features of the data. Figure 7.4 shows a scan of interrogation time T in the range 500μs to

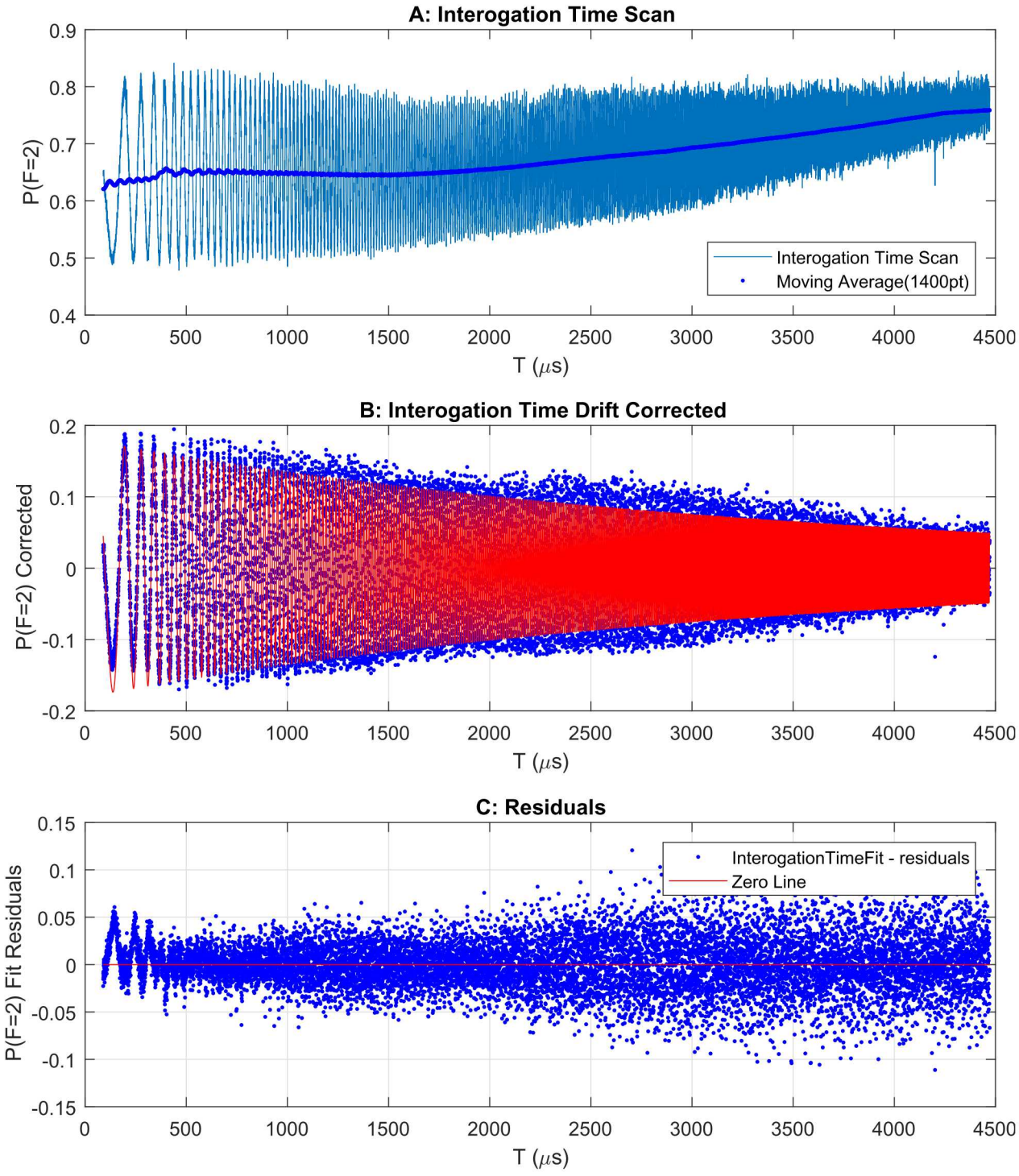

Figure 7.3: Plot A shows the raw results from an Interrogation time scan and an overlaid 1400-point moving average used to remove the offset. This corrected data is shown in plot B along with the result of a fit of the form equation 7.2. Plot C shows the residuals of this fit. The following experimental parameters were used: $t_\pi = 8\mu s$, Raman carrier detuning of $\Delta = -37$GHz (i.e. red) of the rempump laser, with 180mW in the down-going Raman beam and 250mW in the up-going.

1500μs. The fit tracks the periodicity of the oscillations exactly, but has some mismatch in amplitude. Figure 7.5 is still tracking the periodicity of the oscillations, but the contrast is reduced, the amplitude mismatch has grown, and the residuals are approaching the amplitude of the oscillations. These two plots illustrate that the fit successfully matches the period of the oscillations.

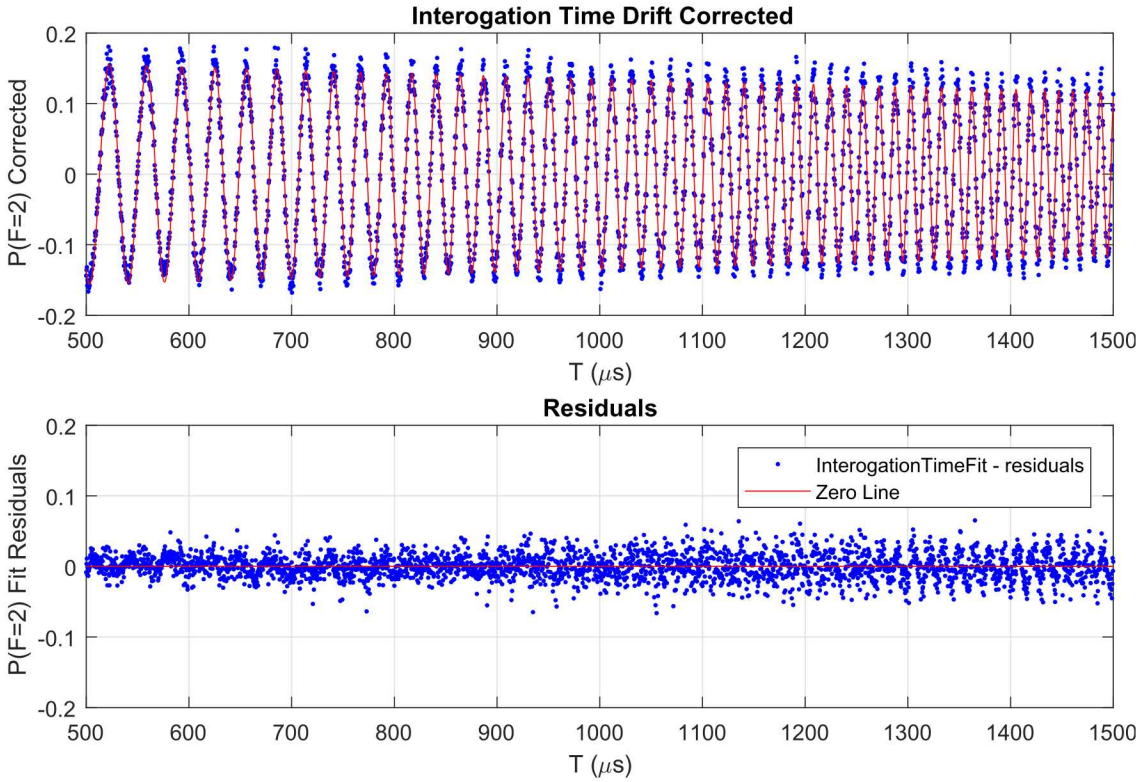

Figure 7.4: T-time (500μs to 1500μs) against drift corrected population with the fit and residuals shown.

The reduction in contrast at longer T-times is believed to be caused by phase noise introduced between the two fibres delivering the Raman beams to the experiment. Thermally and mechanically stressing these fibres cause phase fluctuations that completely obscure fringes at $T = 2$ms. A fast optical phase lock after the fibres would reduce this phase noise and allow the experiment to operate at long T-times, enhancing sensitivity.

The trial function used in figure 7.3B is: (all times are in microseconds)

$$f(x) = a_1 e^{-a_2 x} \sin\left[b_1\left(x^2 + t_\pi\left(1 + \frac{2}{\pi}\right)x\right) + b_2\right] \tag{7.3}$$

Coefficients and 95% confidence bounds are shown in table 7.4.

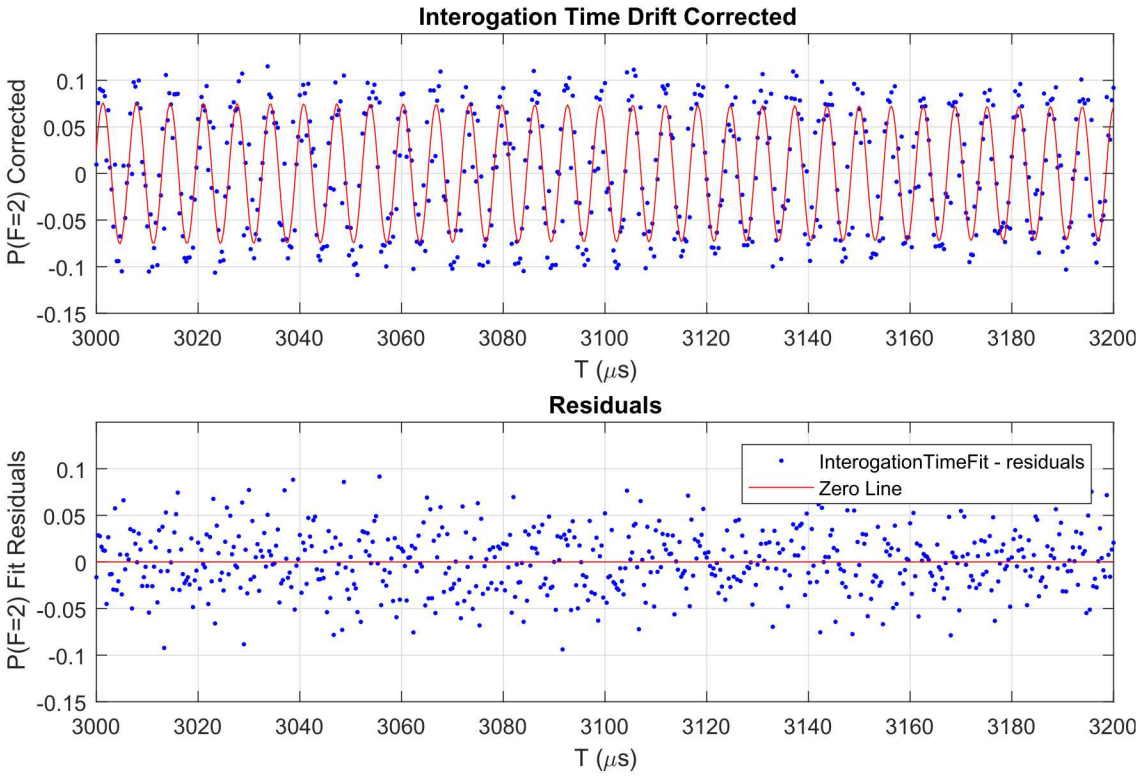

Figure 7.5: T-time (3000μs to 3500μs) against drift corrected population with the fit and residuals shown. Note the change in axis scales when compared to figure 7.4.

Coefficient	Value	95% Confidence interval		
a1	0.1808	0.1789	0.1826	
a2	2.899	2.843	2.955	$\times 10^{-4}$
b1	1.576668	1.576654	1.576682	$\times 10^{-4}$
b2	1.44	1.432	1.447	

Table 7.1: Fit coefficients for equation 7.3

Comparing equation 7.2 and equation 7.3 reveals that b_1 can be used to calculate $g\cos(\theta)$. Making the appropriate substitutions gives:

$$g\cos(\theta) = 9.79039 \pm 4 \times 10^{-5}\,\mathrm{ms}^{-2} \tag{7.4}$$

The above bounds correspond to the 1-σ_g confidence interval and are based entirely on uncertainties in the fit. They should be taken as an indication of measurement precision rather than accuracy. We have not characterised the possible systematics here. The error in $g\cos\theta$ has been taken to match the 1-σ uncertainty in b1; the uncertainties in k_{eff} and T are significantly smaller than the reported uncertainty in $g\cos\theta$ so this

is reasonable.

7.5 Temperature

The Doppler sensitive nature of the Raman pulses allows us to use them to measure the temperature of our atoms source.[43] We follow the method of Wu [18]. Recall the Ramsey sequence $\frac{\pi}{2} \rightarrow \pi \rightarrow \frac{\pi}{2}$ where the pulses are separated by the interrogation time T. We vary the second interrogation time period $T_2 \rightarrow T_2 + \delta T$ causing the interferometer to fail to close. We observe a Gaussian contrast envelope in δT:

$$\chi = \exp\left(-\frac{\delta T^2}{2/(k_{\text{eff}} v_{\text{rms}})^2}\right) \tag{7.5}$$

Where v_{rms} is the one-dimensional RMS velocity of the cloud in the direction of the Raman beams. The one dimensional temperature T_a is given by: [30]

$$T_a = \frac{m v_{\text{rms}}^2}{k_B} \tag{7.6}$$

Figure 7.6 shows such a δT scan showing sinusoidal oscillations in δT with the expected Gaussian envelope. Using equation 7.6 we find $T_a = 1.9\mu$K. This temperature was surprisingly low given the fact that sub-Doppler cooling had not been optimised. The cause of this anomaly was velocity selection from the long pulse time $t_\pi = 8\mu s$. The effective linewidth and resulting velocity class addressed by a Doppler sensitive Raman pulse is determined by the pulse duration. Equation 7.7 states this relationship, where $\sigma_{t\pi}$ is the $1/\sqrt{e}$ width of a Gaussian pulse.[15] In figure 7.6, $t_\pi = 8\mu$s corresponds to a Doppler width of $T_D \simeq 2\mu$K, consistent with both the measured temperature and the fact that velocity selection was responsible.

$$T_{\text{Doppler}} = \frac{m}{k_B (k_{\text{eff}} \sigma_{t_\pi})^2} \tag{7.7}$$

To address the full velocity distribution a shorter pulse was needed. Unfortunately the loss in contrast at long T-times with short pulse lengths prevents us from taking a single shot measurement. Instead we take a phase scan at several values of δT and measure the contrast of each scan. Plotting fringe visibility against δT allows us to measure the Gaussian envelope, at T-times too short to facilitate single shot measurement (100μs in this case). Whilst long T times can result in lower measured temperatures, with hotter atoms leaving the interferometry region, this does not occur in this case. For the the 5.4ms total free-fall time used in figure 7.6, this effect becomes significant for temperatures above 1mK (i.e. 100 times hotter).

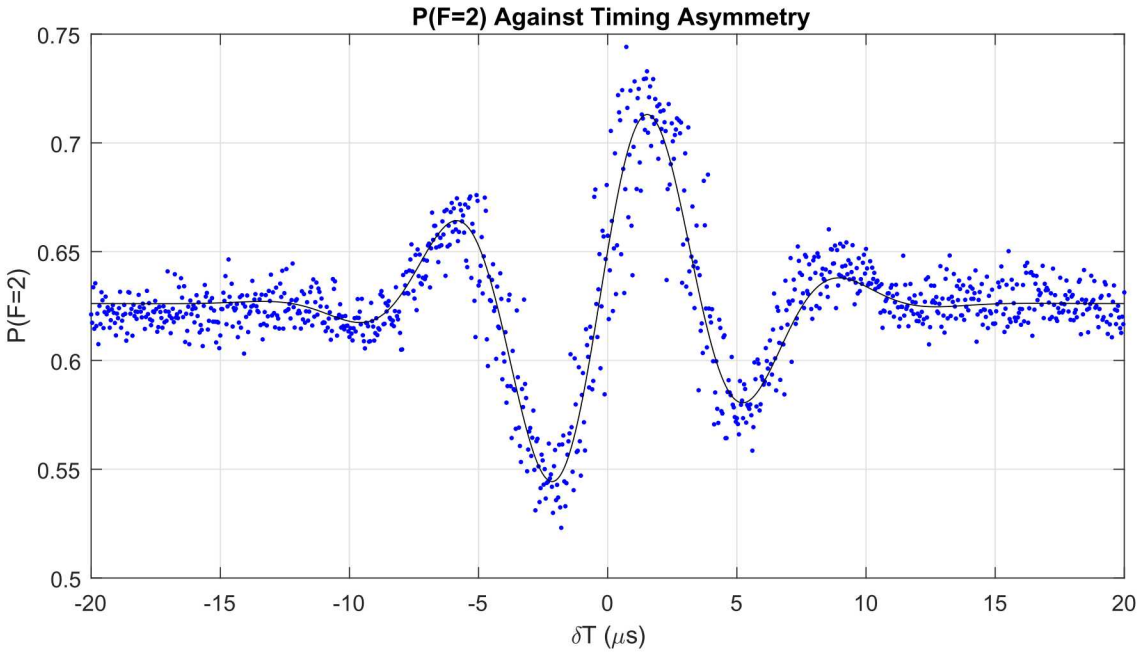

Figure 7.6: A scan of δT against population transfer efficiency. The fit indicates a cloud temperature of 1.9μK. For this scan $T = 2.7$ms. The same experimental parameters were used as in the interrogation time scan figure 7.3.

Figure 7.7 was taken with $t_\pi = 2.0\mu$s and indicates a cloud temperature $T_a = 10.9\mu$K. This t_π results in velocity selection in clouds with temperatures above $\sim 30\mu$k so this measurement is limited by the true velocity profile of the cloud. Additional measurements taken at $t_\pi = 1.1\mu$s indicate an almost identical cloud temperature with velocity selection occuring at the $\sim 100\mu$K level, providing further confirmation that 10.9μK is representative of our sample.

Optimisation of our polarisation gradient cooling should allow us to reach cloud temperatures of at least $T_a = 5.5\mu$K [41] as demonstrated by McGuinness et al. in a similar experiment operating at high-bandwidth (over 100Hz). Lower temperatures are routinely achieved but not at high bandwidth.[33]

7.5.1 Large Power and Detuning

The high power of our Raman laser system should facilitate very short pulses or very large detunings (allowing LMT operation). For an interferometer running at short interrogation times, a short π pulse allows us to address a far larger velocity class of atoms, with a corresponding increase in sensitivity. Large detunings reduce the probability of spontaneous emission during the interferometry pulse ($\mathcal{R}_S \propto \Delta^{-2}$). Whilst this does increase fidelity it has limited usefulness for a standard Ramsey interferometry. For large momentum transfer (LMT) interferometers the increase in fidelity is significant. Even a small loss in pulse fidelity

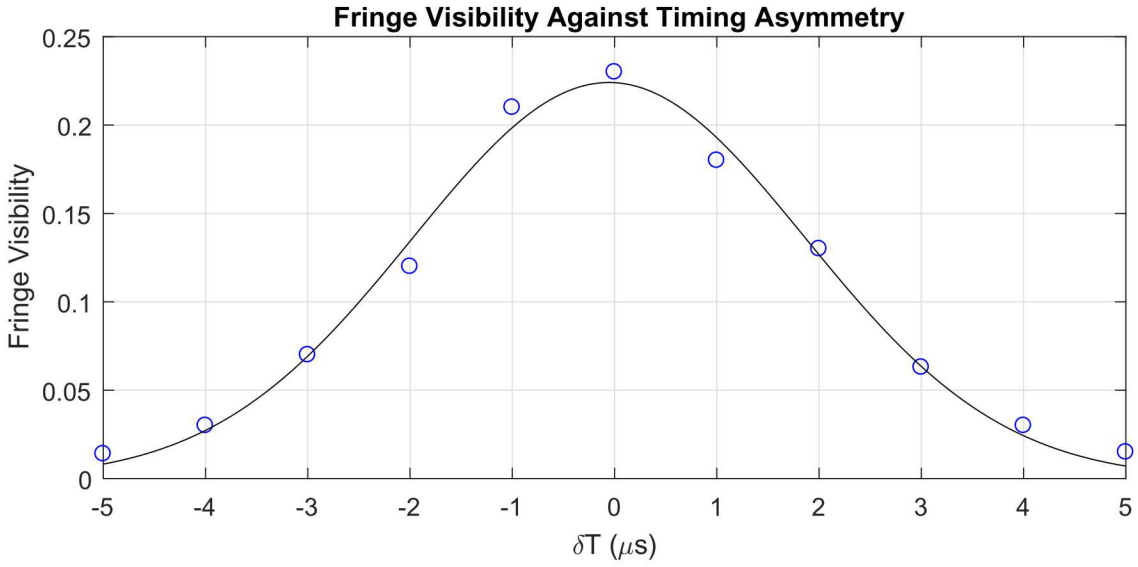

Figure 7.7: A scan of δT against fringe visibility. The Gaussian visibility envelope corresponds to a cloud temperature $T_a = 10.9\mu$K.

very quickly degrades the contrast and sensitivity over the many pulses used for LMT. The potential sensitivity enhancement offered by LMT motivates additional work to consider it's use in this high bandwidth system.[44][45]

CHAPTER 8

CONCLUSION

We have demonstrated a laboratory based, high bandwidth atom interferometer instrument and have performed an incipient gravity measurement with a fractional statistical uncertainty of $\sigma_g/g = 4.4 \times 10^{-6}$ where g is the acceleration due to gravity. This instrument will act as a platform for exploring the fundamental limitations of atom interferometer techniques. The dominant noise source is phase noise between the two Raman beams induced by vibration, stress, and thermal effects in their respective fibres. Significant improvements can follow from the addition of a phase lock on the Raman beam delivery. Finalisation of the proposed cooling and detection laser will further increase performance due to enhanced frequency stability and increased power. The construction of a powerful Raman laser allows an investigation into Raman pulse parameters with much larger single-photon Raman detuning and larger Rabi frequencies, both of which can enhance the atom-optical pulse efficiency. The improvements will enable large momentum transfer, matter-wave beamsplitters that can increase sensitivity for a given T-time. This regime has not been explored at high bandwidth before.

APPENDIX A

ATOMIC STRUCTURE OF RUBIDIUM

The following two figures show the relevant energy levels of rubidium 87 and the transitions addressed by each of the laser beams. The polarisation state of the lasers is also shown.

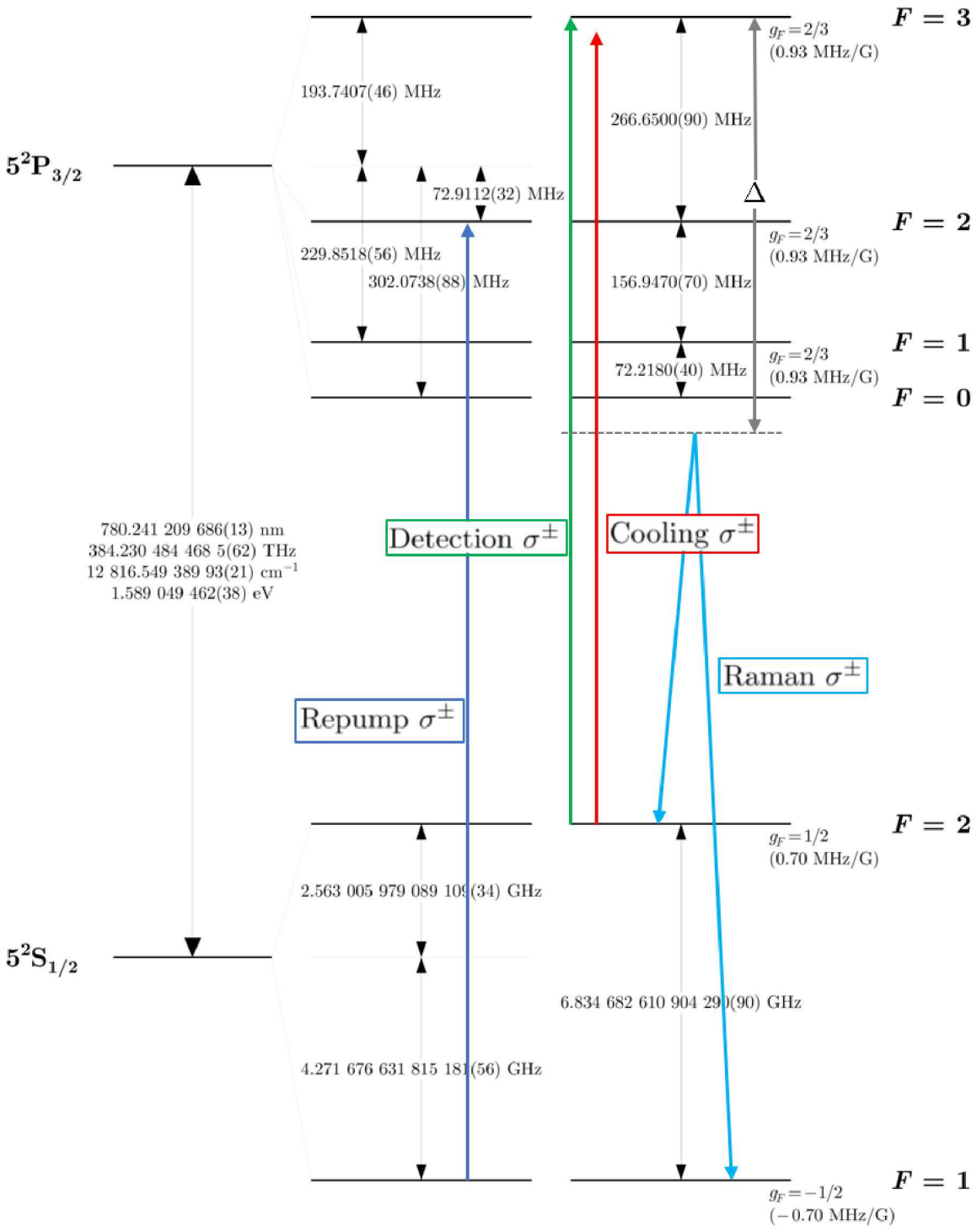

Figure A.1: Rubidium 87 D_2 transition hyperfine structure, with the transitions addressed by the lasers indicated. The polarisations of the lasers are indicated in their labels. Where two polarisations are indicated e.g. $\sigma^{\pm}$, the atoms see light in both polarisations from different beams operating at the indicated frequency. Diagram adapted from Steck.[24]

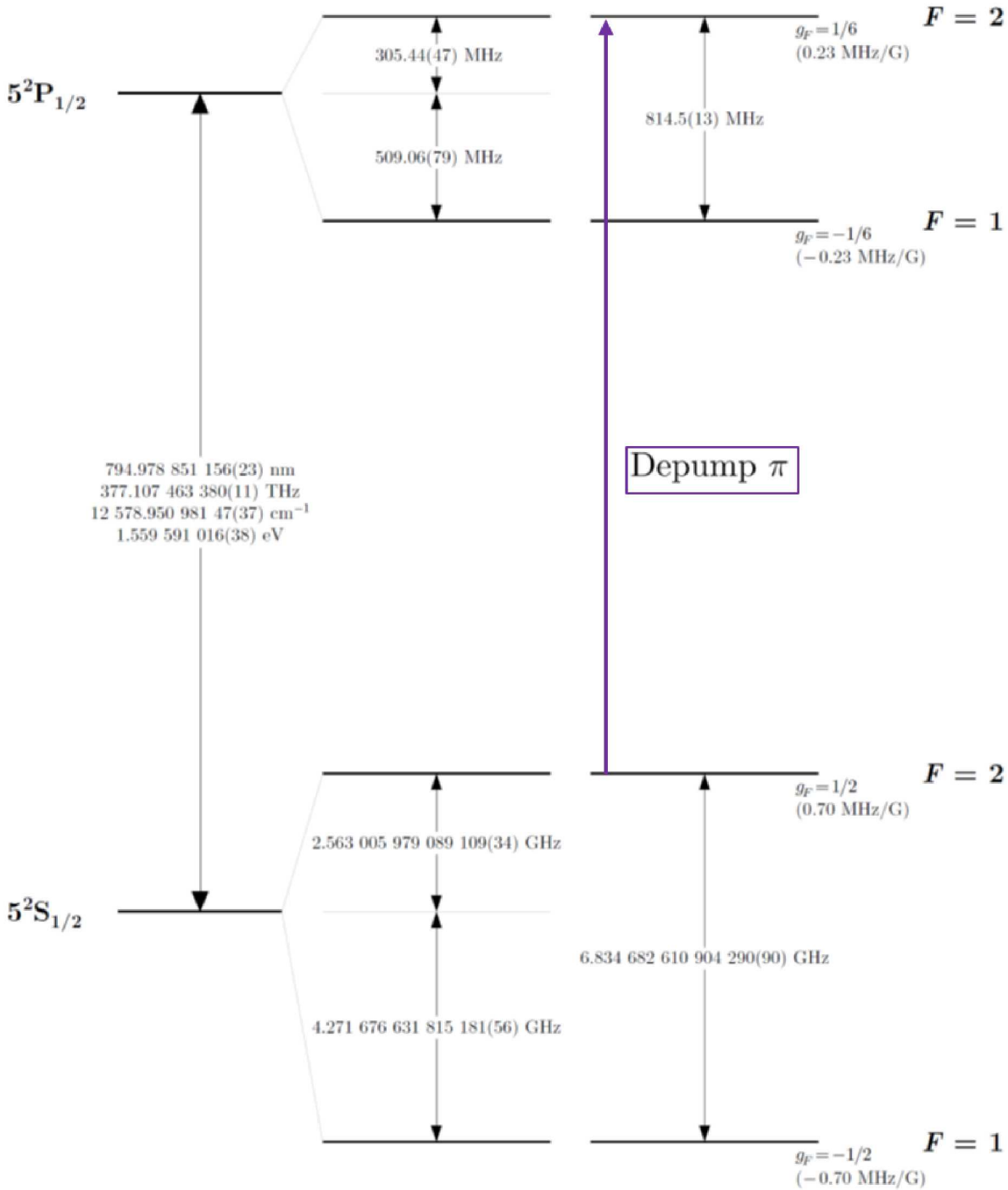

Figure A.2: Rubidium 87 D_1 transition hyperfine structure, with the depump laser indicated by the arrow. The depump laser is π-polarised. The $|F = 2, m_F = 0\rangle$ sublevel is dark to this laser. As a result atoms are shelved to this level during optical pumping. Diagram adapted from Steck.[24]

LIST OF REFERENCES

[1] Louis De Broglie. *Recherches sur la théorie des quanta*. PhD thesis, Migration-université en cours d'affectation, 1924.

[2] Richard H Parker, Chenghui Yu, Weicheng Zhong, Brian Estey, and Holger Müller. Measurement of the fine-structure constant as a test of the standard model. *Science*, 360(6385):191–195, 2018.

[3] Jeffrey B Fixler, GT Foster, JM McGuirk, and MA Kasevich. Atom interferometer measurement of the newtonian constant of gravity. *Science*, 315(5808):74–77, 2007.

[4] Michael A Hohensee, Holger Müller, and RB Wiringa. Equivalence principle and bound kinetic energy. *Physical review letters*, 111(15):151102, 2013.

[5] Michael A Hohensee, Brian Estey, Paul Hamilton, Anton Zeilinger, and Holger Müller. Force-free gravitational redshift: proposed gravitational aharonov-bohm experiment. *Physical Review Letters*, 108(23):230404, 2012.

[6] T Kovachy, P Asenbaum, C Overstreet, CA Donnelly, SM Dickerson, A Sugarbaker, JM Hogan, and MA Kasevich. Quantum superposition at the half-metre scale. *Nature*, 528(7583):530, 2015.

[7] A Einstein. Über das relativitätsprinzip und die aus demselben gezogene folgerungen, (on the relativity principle and the conclusions drawn from it). *Jahrbuch der Radioaktivitfit and Elektronik*, 4:411–462, 1907.

[8] A Albarbar, Abdellatef Badri, Jyoti K Sinha, and A Starr. Performance evaluation of MEMS accelerometers. *Measurement*, 42(5):790–795, 2009.

[9] Oliver J Woodman. An introduction to inertial navigation. Technical report, University of Cambridge, Computer Laboratory, 2007.

[10] B Canuel, F Leduc, D Holleville, A Gauguet, J Fils, A Virdis, A Clairon, N Dimarcq, Ch J Bordé, A Landragin, et al. Six-axis inertial sensor using cold-atom interferometry. *Physical review letters*, 97(1):010402, 2006.

[11] Christopher Jekeli. Navigation error analysis of atom interferometer inertial sensor. *Navigation*, 52(1):1–14, 2005.

[12] Akash V Rakholia, Hayden J McGuinness, and Grant W Biedermann. Dual-axis high-data-rate atom interferometer via cold ensemble exchange. *Physical Review Applied*, 2(5):054012, 2014.

[13] QT Hub. Uk quantum technology hub for sensors and metrology. https://www.quantumsensors.org/innovation/activities/gravity-sensors/. Accessed: 2018-03-25.

[14] LP Peters, Jeffrey J Daniels, and Jonathan D Young. Ground penetrating radar as a subsurface environmental sensing tool. *Proceedings of the IEEE*, 82(12):1802–1822, 1994.

[15] Malte Schmidt. *A mobile high-precision gravimeter based on atom interferometry*. PhD thesis, Humboldt-Universität zu Berlin, Mathematisch-Naturwissenschaftliche Fakultät I, 2011.

[16] Susannah M. Dickerson, Jason M. Hogan, Alex Sugarbaker, David M. S. Johnson, and Mark A. Kasevich. Multiaxis inertial sensing with long-time point source atom interferometry. *Phys. Rev. Lett.*, 111:083001, Aug 2013.

[17] Mark A Kasevich. *Atom interferometry in an atomic fountain*. PhD thesis, Stanford University, 1992.

[18] Xinan Wu. *Gravity gradient survey with a mobile atom interferometer*. PhD thesis, Stanford University, 2009. Chapter 3.2.

[19] Akash Rakholia. *High Data-Rate Atom Interferometry for Measuring Dynamic Inertial Conditions*. PhD thesis, The University of New Mexico, 2015.

[20] Jeffrey Michael McGuirk. *High precision absolute gravity gradiometry with atom interferometry*. PhD thesis, PhD thesis, Stanford University, 2001.

[21] SS Sané, S Bennetts, JE Debs, CCN Kuhn, GD McDonald, PA Altin, JD Close, and NP Robins. 11 w narrow linewidth laser source at 780nm for laser cooling and manipulation of rubidium. *Optics express*, 20(8):8915–8919, 2012.

[22] GD Boyd and DA Kleinman. Parametric interaction of focused gaussian light beams. *Journal of Applied Physics*, 39(8):3597–3639, 1968.

[23] Alexander Franzen. Component library. http://www.gwoptics.org/ComponentLibrary/. Licensed under a Creative Commons Attribution-NonCommercial 3.0 Unported License.

[24] Daniel A Steck. Rubidium 87 d line data, (revision 2.1. 5, 13 january 2015). *http://steck.us/alkalidata*, 2001.

[25] Daniel A Steck. Rubidium 85 d line data, (revision 2.1.6, 20 september 2013). *http://steck.us/alkalidata*, 2008.

[26] Theodor W Hänsch and Arthur L Schawlow. Cooling of gases by laser radiation. *Optics Communications*, 13(1):68–69, 1975.

[27] Alan L Migdall, John V Prodan, William D Phillips, Thomas H Bergeman, and Harold J Metcalf. First observation of magnetically trapped neutral atoms. *Physical Review Letters*, 54(24):2596, 1985.

[28] Steven Chu, Leo Hollberg, John E Bjorkholm, Alex Cable, and Arthur Ashkin. Three-dimensional viscous confinement and cooling of atoms by resonance radiation pressure. *Physical review letters*, 55(1):48, 1985.

[29] EL Raab, M Prentiss, Alex Cable, Steven Chu, and David E Pritchard. Trapping of neutral sodium atoms with radiation pressure. *Physical Review Letters*, 59(23):2631, 1987.

[30] Harold J Metcalf and Peter Van der Straten. *Laser Cooling and Trapping*. Springer, 1999.

[31] Harold Metcalf. Magneto-optical trapping and its application to helium metastables. *JOSA B*, 6(11):2206–2210, 1989.

[32] C Chesman, EG Lima, FAM De Oliveira, SS Vianna, and JWR Tabosa. Two-and four-beam magneto-optical trapping of neutral atoms. *Optics letters*, 19(16):1237–1239, 1994.

[33] Quentin Bodart, Sébastien Merlet, Nicola Malossi, F Pereira Dos Santos, Philippe Bouyer, and Arnaud Landragin. A cold atom pyramidal gravimeter with a single laser beam. *Applied Physics Letters*, 96(13):134101, 2010.

[34] Jeffrey Michael Mcguirk, GT Foster, JB Fixler, MJ Snadden, and MA Kasevich. Sensitive absolute-gravity gradiometry using atom interferometry. *Physical Review A*, 65(3):033608, 2002.

[35] Yuan-Yu Jau and Jongmin Lee. Microfabricated waveguide atom traps. *Sandia National Laboratories*, 2017.

[36] E. Vetsch, D. Reitz, G. Sagué, R. Schmidt, S. T. Dawkins, and A. Rauschenbeutel. Optical interface created by laser-cooled atoms trapped in the evanescent field surrounding an optical nanofiber. *Phys. Rev. Lett.*, 104:203603, May 2010.

[37] A. Goban, K. S. Choi, D. J. Alton, D. Ding, C. Lacroûte, M. Pototschnig, T. Thiele, N. P. Stern, and H. J. Kimble. Demonstration of a state-insensitive, compensated nanofiber trap. *Phys. Rev. Lett.*, 109:033603, Jul 2012.

[38] Xinye Xu, V. G. Minogin, Kwanil Lee, Yuzhu Wang, and Wonho Jhe. Guiding cold atoms in a hollow laser beam. *Phys. Rev. A*, 60:4796–4804, Dec 1999.

[39] S. J. M. Kuppens, K. L. Corwin, K. W. Miller, T. E. Chupp, and C. E. Wieman. Loading an optical dipole trap. *Phys. Rev. A*, 62:013406, Jun 2000.

[40] Gregory W Hoth, Elizabeth A Donley, and John Kitching. Atom number in magneto-optic traps with millimeter scale laser beams. *Optics letters*, 38(5):661–663, 2013.

[41] Hayden J McGuinness, Akash V Rakholia, and Grant W Biedermann. High data-rate atom interferometer for measuring acceleration. *Applied Physics Letters*, 100(1):011106, 2012.

[42] Achim Peters. *High Precision Gravity Measurements Using Atom Interferometry*. PhD thesis, Stanford University, 1998.

[43] Mark Kasevich, David S Weiss, Erling Riis, Kathryn Moler, Steven Kasapi, and Steven Chu. Atomic velocity selection using stimulated raman transitions. *Physical review letters*, 66(18):2297, 1991.

[44] JM McGuirk, MJ Snadden, and MA Kasevich. Large area light-pulse atom interferometry. *Physical review letters*, 85(21):4498, 2000.

[45] Sheng-wey Chiow, Tim Kovachy, Hui-Chun Chien, and Mark A Kasevich. $102\hbar k$ large area atom interferometers. *Physical review letters*, 107(13):130403, 2011.